



Perovskite/silicon tandem solar cells—compositions for improved stability and power conversion efficiency

Charles Marchant¹ · René M. Williams¹

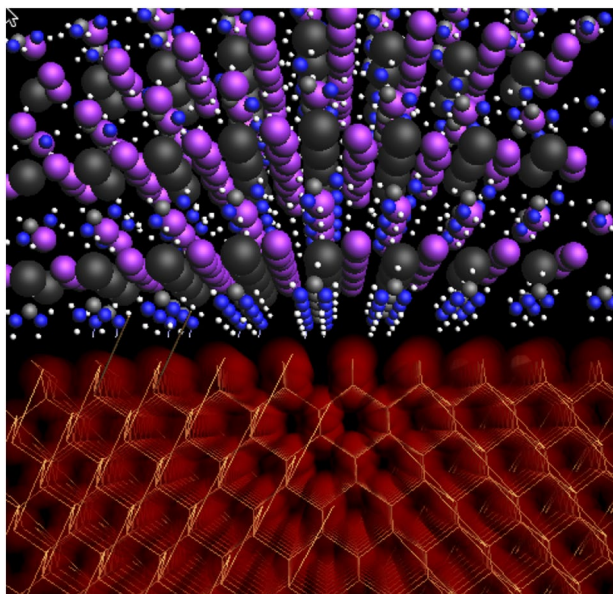
Received: 14 April 2023 / Accepted: 23 October 2023 / Published online: 22 November 2023

© The Author(s), under exclusive licence to European Photochemistry Association, European Society for Photobiology 2023

Abstract

Perovskite/Silicon Tandem Solar Cells (PSTSCs) represent an emerging opportunity to compete with industry-standard single junction crystalline silicon (c-Si) solar cells. The maximum power conversion efficiency (PCE) of single junction cells is set by the Shockley–Queisser (SQ) limit (33.7%). However, tandem cells can expand this value to ~45% by utilising two stacked solar cells to harvest the solar spectrum more efficiently. 33.9% PCE has already been achieved with PSTSCs. This perspective analyses recent advances in PSTSC technology, with an emphasis on optimal perovskite composition, the problem and mitigation of light-induced halide phase segregation, self-assembled hole transporting monolayers and additives that can improve and stabilise the perovskite. Top-performing compositions show three cationic components (Cs^+ , FA^+ , Pb^{2+}) and three anionic (I^- , Br^- , Cl^-) with a bandgap between 1.55 and 1.77 eV and a theoretical maximum of 1.73 eV (717 nm). Anionic additives such as $(\text{Br}_3)^-$ and SCN^- reduce trap states and segregation. 2D-perovskite grain boundary interfaces are created with cationic alkylammonium additives such as methyl-phenethylammonium (MPEA) and result in improved performance. 2-, 3- or 4-terminal devices with a (partly) textured silicon heterojunction (SHJ) bottom cell are ideal. An ultra-thin interfacial recombination layer (~5 nm) of indium tin oxide (ITO) or indium zinc oxide (IZO) containing a carbazole-based hole transporting self-assembled monolayer (Me-4PACz) is used for optimal 2-terminal tandem devices.

Graphical Abstract



Perspective Topical Collection in honor of Prof. Dr. A. M. (Fred) Brouwer and his contributions to science.

Extended author information available on the last page of the article

Keywords Solar energy conversion · Charge generation · Lead halide perovskite · Formamidinium · Additives · Alkylammonium

Abbreviations

2 T, 3 T, 4 T	Two, three, four Terminal
a-Si	Amorphous silicon
a-Si:H	Hydrogenated amorphous silicon
CIGS	Copper Indium Gallium diSelenide
c-Si	Crystalline Silicon
CTL	Charge Transport Layer
Cz	Czochralski
ETL	Electron Transport Layer
EQE	External Quantum Efficiency
FF	Fill Factor
FZ	Float-Zone
HTL	Hole Transport Layer
IBC	Interdigitated Back Contact
IR	Infrared
Jsc	Short-Circuit Current Density
mc-Si	Multicrystalline silicon
nc-Si	Nanocrystalline silicon
NIR	Near-IR
NREL	National Renewable Energy Laboratory
PCE	Power Conversion Efficiency
PERC	Passivated Emitter Rear Cell
PL	Photoluminescence
PSC	Perovskite Solar Cell
PSTSC	Perovskite/Si Tandem Solar Cell
PV	Photovoltaic
RL	Recombination Layer
SAM	Self-Assembling Monolayer
SHJ	Silicon Heterojunction
SQ	Shockley-Queisser
TCO	Transparent Conductive Oxide
TJ	Tunnel Junction
TSC	Tandem Solar Cell
UV	Ultraviolet
Voc	Open-Circuit Voltage

Chemicals

2PACz	(2-(9H-carbazol-9-yl)ethyl)phosphonic acid
4-MPEA	4-Methylphenethylammonium
ADDC	Ammonium diethyldithiocarbamate
BA	Butylammonium
BHC	Benzylhydrazine hydrochloride
FA	Formamidinium—HC(NH ₂) ₂
ITO	Indium doped Tin Oxide
MA	Methylammonium—CH ₃ NH ₃

MeO-4PACz	(4-(3,6-Dimethoxy-9H-carbazol-9-yl)butyl)phosphonic acid
Me-4PACz	4-(3,6-Dimethyl-9H-carbazol-9-yl)butyl]phosphonic Acid
PCBM	[6, 6]-phenyl-C ₆₁ -butyric acid methyl ester
PEA	Phenethylammonium
PEDOT-PSS	Poly(3,4-ethylenedioxythiophene) polystyrene sulfonate
PI	Piperazinium iodide
PTAA	Poly[bis(4-phenyl)(2,4,6-trimethylphenyl)amine
spiro-OMeTAD	2,2',7',7'-Tetrakis(N,N-di-p-methoxyphenyl amine)-9,9'-spirobifluorene
TEA	Thiophene-ethylammonium
TMA	Thiophene-methylammonium
TPA	Trimethylphenylammonium
ZTO	Zinc doped Tin Oxide

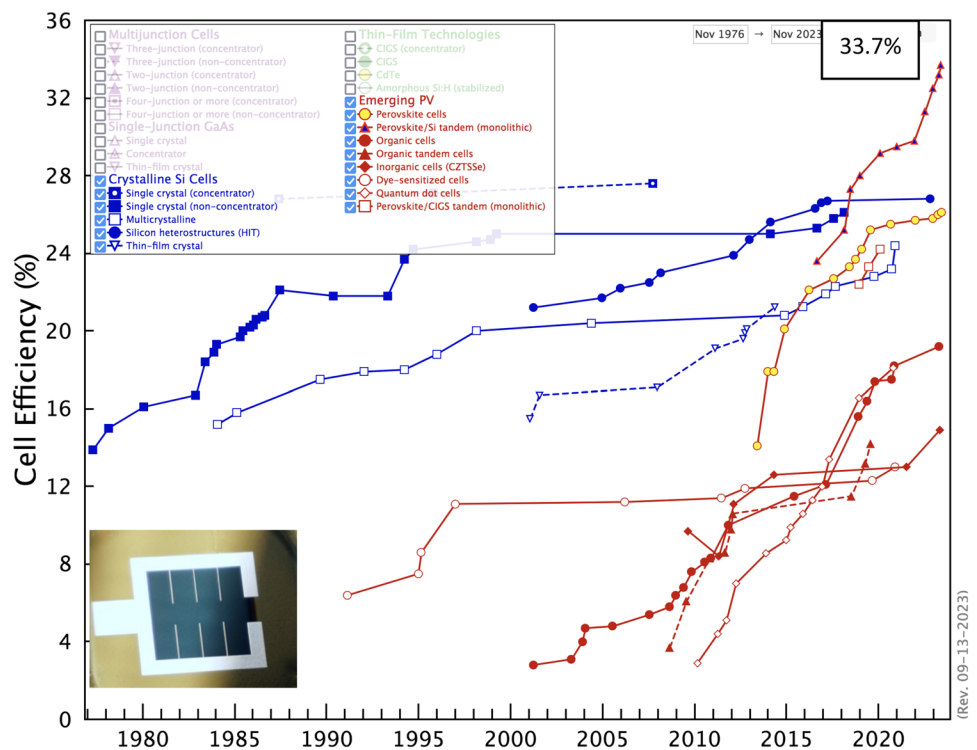
1 Introduction

As the global human population continues to grow and living standards rise, the demand for energy is increasing faster than ever before. To date, our energy demands have primarily been met with fossil fuels, however, owing to their contribution to climate change and their finite nature, our future energy demand must be linked to clean, renewable resources. Among the renewable energy sources being increasingly adopted, such as wind, hydroelectric and geothermal energy, solar photovoltaic (PV) energy in particular offers abundant clean energy, utilising sunlight as the energy source [1]. As a result, photovoltaic devices are being adopted to an increasing extent for large-scale energy production [2].

Commercial solar cells predominantly use silicon (Si) as the semiconducting material, comprising 95% of the market [3]. However, the power conversion efficiency (PCE) of single junction solar cells is restricted to 33.7% by the Shockley-Queisser (SQ) limit [4], but realistically is limited to 29.4% when taking Auger recombination into account [5]. In reality, crystalline silicon (c-Si) solar cell PCE has plateaued at around 26–27% for the past decade, with the current record at 26.1% for single crystal Si (non-concentrated sunlight) and 26.8% for Si heterostructures (HIT: Heterojunction with Intrinsic Thin-film) (Fig. 1) [6].

Tandem solar cells (TSCs) offer a route to increasing the PCE by stacking solar cells to capture more of the incident

Fig. 1 Best research cell efficiencies of crystalline Si cells (blue) and emerging PV technologies (red) compiled by the National Renewable Energy Laboratory (NREL) [6]. This picture is best viewed on-screen or on the NREL website. Inset shows the 32.5% PCE device of HZB (Helmholtz-Zentrum Berlin)



sunlight and convert it into electrical power. By stacking two solar cells with different bandgaps, the theoretical limit is raised to ~45% PCE [7–9]. The cell on top should have a wide bandgap to absorb high-energy photons, while transmitting low-energy photons to the bottom cell. Perovskite solar cells (PSCs) have emerged as a popular top cell. Any material with a suitable bandgap can be employed as a bottom cell and a variety of materials are being researched as such [10, 11]. of these, silicon is the most promising owing to its widespread use in commercial solar cells, robust nature and natural abundance. Figure 1 shows the rise in PCE of PSCs (yellow circles) in a short period in time, taken over by the increasing PCE in perovskite/silicon TSCs (PSTSCs) (purple triangles). PSTSC research has shown remarkable progress in the last few years, owing primarily to the rise in efficiency of single junction PSCs.

This work will focus on the prospects and recent advancements in PSTSC technology. First, relevant background information on single junction PSCs and Si cells will be presented, followed by an explanation of the working principal of TSCs. The main components will be discussed with reference to the key requirements for an efficient and stable cell. The different configurations of TSCs will be introduced, and the benefits and challenges associated with each type will be explored.

The main body of this work will discuss reports in the literature (primarily since 2020, published until 28 September 2023) with an emphasis on methods employed to overcome key challenges and improve efficiency. Particularly, the focus

is on fine-tuning the perovskite composition to minimise detrimental effects on the stability, such as halide phase segregation, while maintaining an appropriate bandgap for optimal performance and PCE. Important main components of the perovskite top cell will be elucidated, including the effects of changing the perovskite composition, particularly on the bandgap and the stability, as well as the effects of additives on defects [12] and segregation. The benefits and drawbacks of n-i-p vs. p-i-n architectures will also be treated (see Fig. 2). Various aspects of the silicon bottom cell will be explored, including the type of silicon used, the treatment applied to it, and the effect of texturing the surface to improve light harvesting. The interface between the two sub-cells will also be examined. The typical charge transport layers (CTLs) and their associated benefits and drawbacks, and the transparent conductive electrodes (TCOs) will be discussed. Finally, the findings will be summarised, the future prospects and the state-of-the-art of PSTSCs will be evaluated and avenues for future research will be presented.

2 Background information

The term ‘perovskite’ was first used to describe the mineral calcium titanite, with a formula CaTiO_3 . The term has since been used to describe any compound with the generic formula ABX_3 , with a crystal structure as shown in Fig. 2a. In 2009, the first perovskite solar cell (PSC) was reported, using $\text{CH}_3\text{NH}_3\text{PbI}_3$ and $\text{CH}_3\text{NH}_3\text{PbBr}_3$ perovskite nanocrystals to

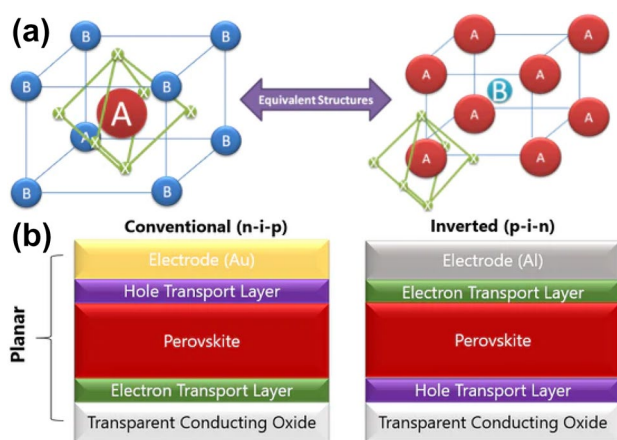


Fig. 2 **a** Diagram of the crystal structure of perovskite. **b** General schematic of a PSC, both with conventional n-i-p architecture and inverted p-i-n architecture [19]. Note that in the p-i-n architecture the hole transport layer (p) is on the transparent conductive oxide. The perovskite is the intrinsic layer (i) and the electron transport layer (n) is similar to an n-doped material

sensitize TiO_2 , building on the principle of dye-sensitized solar cells (DSSCs). This cell was able to convert sunlight into electrical power with a PCE of 3.8% [13].

Since this first reported PSC, the record PCE has grown remarkably to 26.1% in 2023, which is almost as high as the single junction Si record PCE of 26.8% [6]. The current state-of-the-art PSCs use thin film crystalline perovskites, generally using an organic (methylammonium–MA, or formamidinium–FA) or alkali metal (Cs or Rb) cation in the A position, lead (or tin) in the B position, and halides in the X position. In early PSCs, mesoporous TiO_2 would act as a scaffold for perovskite crystals and extract electrons, with holes being extracted by a liquid iodine-based electrolyte, however, these latter materials were soon replaced with discrete CTLs [14], as shown in Fig. 2b. The majority of PSCs use an n-i-p, or ‘conventional’ architecture, with 2,2',7',7'-tetrakis(*N,N*-di-*p*-methoxyphenyl amine)-9,9'-spirobifluorene (spiro-OMeTAD) as the hole transport layer (HTL) [15], and TiO_2 or SnO_2 as the electron transport layer (ETL) [14]. For ‘inverted’, or p-i-n devices, the HTL may be a polymeric structure such as PEDOT:PSS [16] or PTAA [17], or an inorganic oxide such as NiO [18], while the ETL is typically fullerene (C_{60}) or a derivative such as PCBM. [14].

While the growth of PSCs over the past decade is remarkable, the PCE of these cells is still fundamentally limited by the SQ limit of 33.7%, which is an intrinsic limit to single junction solar cells [4, 20, 21]. To further push the PCE of solar cell towards this limit and beyond, solar cells with multiple junctions must be developed. For a hypothetical cell with infinite junctions, the SQ limit can rise to 68% for unconcentrated sunlight [22], but for practical applications,

a two-junction TSC with a limit of 44.8% [7, 23] could represent a ~30% increase in energy yield compared to single junction solar cells. This upper limit is calculated on the basis of a free choice of bandgap. Ideally, the bandgap of the bottom cell should be 0.96 eV (mainly absorbing near-IR photons), and the top cell 1.63 eV (mainly absorbing UV–Visible photons). While any two semiconducting materials can be employed as top and bottom cells in a TSC, c-Si is an ideal bottom cell, owing to its market dominance and an appropriate bandgap of 1.12 eV. With this bandgap, the ideal top cell bandgap is 1.73 eV, giving a theoretical efficiency limit of 44.3% [23]. The top cell absorbs high energy photons and converts their energy into power, while lower energy photons are transmitted to the bottom cell to be absorbed and converted. As such, transparency is a key requirement for PSTSCs, and all top cell layers must have adequate transparency to allow photons to reach the Si bottom cell.

The two sub-cells of the TSC can be connected in a number of different ways. The most commonly reported configuration is the two-terminal (2 T) configuration, sometimes referred to as a monolithic TSC. In this configuration, the perovskite sub cell is deposited directly on top of the c-Si cell, and two electrodes, one at the top and one at the bottom, are used.

In 2 T tandems the two cells are connected in series and therefore can be victim of current limitation. If sub-cell currents are not matched, the lower current dominates (the voltages are added). In principle, power matching conditions of the two cells give optimal output, but this can be simplified by current matching, due to the series connection.

Alternatively, the two sub-cells can be manufactured separately, and then mechanically connected in a four-terminal (4 T) configuration, using four electrodes; one each on the top and bottom of the PSC, and one each on the top and bottom of the c-Si solar cell. Maximum power point tracking can be applied to a 4 T configuration, for each sub-cell. There are benefits and drawbacks to each configuration. The 2 T configuration requires less material, lowering the cost, however, this configuration is subject to current matching, limiting the current to the sub-cell with the lower current, and restraining the choice of top cell bandgap (Fig. 3) [24]. If the bandgap of the perovskite is too high, then it will absorb fewer photons, limiting the current, adversely affecting the bottom cell due to the current matching constraint. Conversely, if the bandgap is too low, then the perovskite will absorb photons that should have been transmitted to the bottom cell, and the current of the silicon sub-cell will be reduced, causing a detrimental cumulative effect to the top cell. The 4 T configuration is not constrained by current matching, however, more materials are required, and in particular, it requires three transparent electrodes rather than one in the 2 T configuration, increasing optical losses.

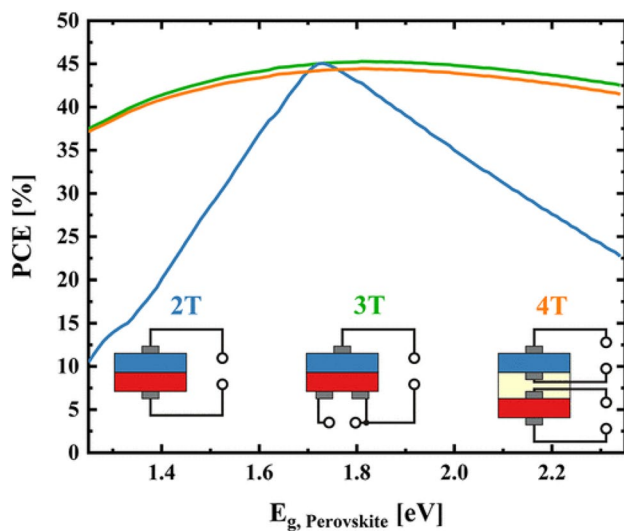


Fig. 3 Basic schematic of 2 T, 3 T and 4 T TSC configurations, with the maximum theoretical PCE as a function of the bandgap of the perovskite (with a c-Si bottom cell bandgap of 1.12 eV). Reprinted with permission from ACS Appl. Energy Mater., 2020, 3, 1381–1392. Copyright 2020 American Chemical Society [24]

4 T devices are also more expensive on the systems level, requiring more peripherals. A third configuration using three terminals (3 T) is also possible, but far less investigated than 2 T or 4 T configurations. The third terminal removes the restraint imposed by current matching while allowing for monolithic fabrication reducing optical losses. This configuration typically employs an interdigitated back contact (IBC) to serve as the second and third electrodes; while a middle third electrode is possible, it is seldom employed, especially in PSTSCs, due to increased optical losses [25]. In both the 4 T and 3 T systems, the lack of a current matching requirement means that a deviation from the ideal bandgap is less detrimental as there is no cumulative (knock-on) effect on the bottom cell's performance.

One of the major advantages of perovskite materials is the tunability of the bandgap. The most common perovskite used in single junction PSCs, MAPbI₃, has a bandgap of 1.55 eV [26], while replacing the iodide with bromide widens the bandgap to 2.3 eV [27]. By mixing bromide and iodide, the bandgap can be tuned closer to the ideal value, however, doing so causes stability issues. The issue of stability is one of the key challenges facing PSCs and PSTSCs, owing to their sensitivity to environmental water and oxygen (which can be mitigated by encapsulation) [28, 29], but also owing to the intrinsic instability of the perovskite material, along with other layers in the cell, particularly in high-temperature working conditions [30]. One of the key issues arising is the phase segregation of iodide and bromide within the perovskite, leading to the generation of trap states causing charge carrier recombination. This is especially pronounced when

the bromide ratio is above 20% [31]. Methods to reduce this effect, including incorporating chloride, and using mixed A site cations, will be explored in this work.

c-Si is an ideal choice for the bottom cell. The bandgap of 1.12 eV is close to the ideal bottom cell value of 0.96 eV. Various different types of c-Si exist for use as a single junction solar cell and for use in a PSTSC. This work will explore the benefits and drawbacks of different types of c-Si cells used as bottom cells, and particular attention will be paid to the effect of texturing the front of the bottom cell, which can improve light harvesting but leads to issues depositing the perovskite top cell.

3 Challenges to overcome

PSTSC research continues to push the PCE higher, tackling major challenges such as improving transparency and reducing optical losses, optimising both the top perovskite and bottom silicon cells, and optimising the various other layers required (including the CTLs, TCO electrodes and interfaces, buffer layers and light management layers). These optimisations have sought to improve both the optical properties and the intrinsic stability, primarily of the top perovskite cell, and will be discussed in this work. Nevertheless, while the PCE continues to be improved, producing PSTSCs with sufficient stability to compete with commercial single junction silicon solar cells (which have a lifetime of approximately 25–30 years) [7, 30] remains challenging. Few long-term stability tests have been performed [32], however, a 2023 review suggests that an 8–10 year lifetime for PSTSCs is achievable in the near future [30]. It should be noted that proper hermetic encapsulation (preventing moisture ingress and outgassing of decomposition products) has been shown to be very beneficial for single-junction perovskite devices, allowing them to pass the International Electrotechnical Commission (IEC) 61,215:2016 Damp Heat and Humidity Freeze tests [33]. In contrast to GaAs-based technology [34, 35] (e.g. Alta-Devices with 31.6% PCE tandem in 2016) [6] the perovskite Si tandem cells do not need to disrupt the current giant Si industry (like David and Goliath), but their manufacture can be integrated into current Si technology (if you can't beat them, join them!). This is manifested by the current activities of e.g. Oxford PV, Meyer Burger, Q-cells / Hanwha and LONGi.

4 Perovskite/Silicon tandem solar cell composition

This section will analyse the composition of the perovskite top cell, and the silicon bottom cell used for PSTSCs. The various effects of adjusting the composition will be

discussed, with an emphasis on minimising destabilising effects. Materials used for the various other layers will also be mentioned, but the main focus of this work will be the composition of the lead halide perovskite, and the silicon bottom cells.

5 Early perovskite/silicon tandem solar cells

The first experimental example of a 2 T PSTSC was reported in 2015 by Mailoa et al. [36]. This early tandem cell (Fig. 4) utilised a MAPbI₃ perovskite with a bandgap of 1.61 eV deposited on a homojunction n-type c-Si cell with a p⁺⁺ Si emitter, with an n⁺⁺ Si tunnel junction (++ implies high doping) as the interface between the two cells. A mesoporous TiO₂ ETL was used, however, they noted substantial optical losses. The same can be said for the spiro-OMeTAD HTL. Following Ag nanowire electrode deposition, a LiF anti-reflection layer was added. The PCE was 13.7%.

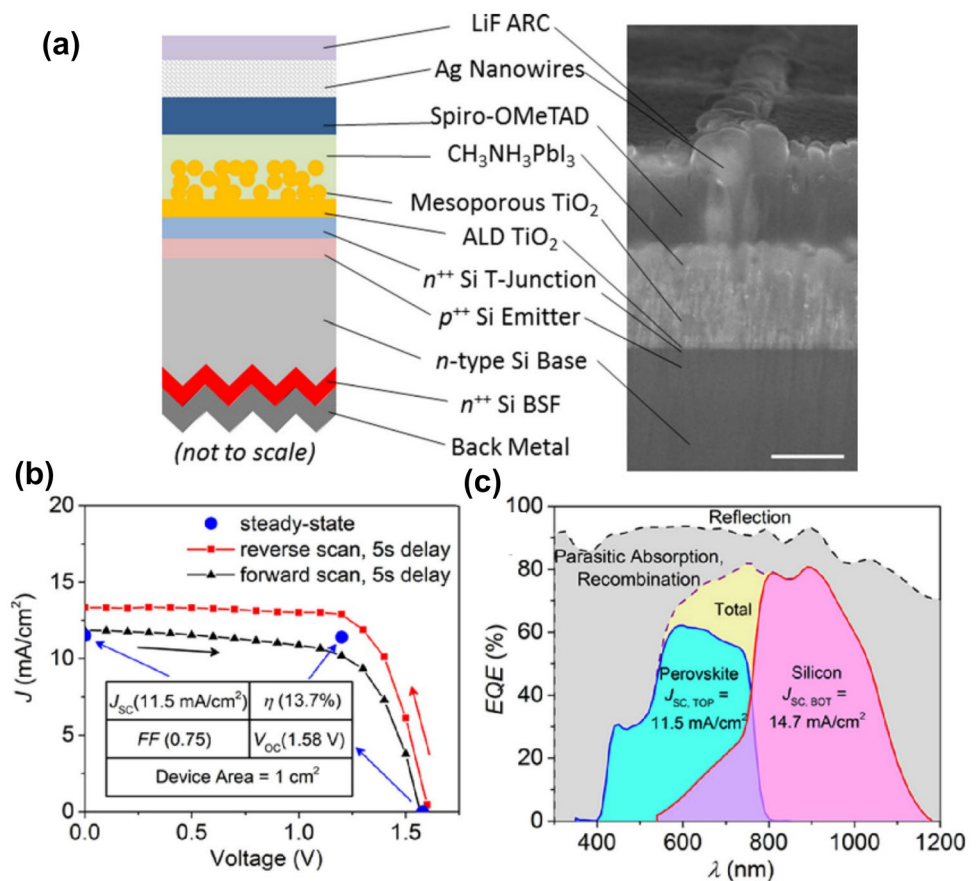
Consecutively, the same group fabricated the first 4 T configured PSTSC [37], also using MAPbI₃ as the perovskite, citing instability observed in bromide-containing perovskites, specifically caused by light-induced halide segregation [31]. Similar to the 2 T cell, the ETL and HTL were mesoporous TiO₂ and spiro-OMeTAD respectively. They

opted to use a low-quality ‘upgraded metallurgical-grade’ multi-crystalline Si (mc-Si) in an effort to test the viability of low-cost silicon for use in a tandem cell. They reported a PCE of 17%, noting that the low-quality mc-Si achieved only 11.4% PCE as a single-junction cell. Nevertheless, the efficiency only improved to 17.9% when a higher-quality silicon bottom cell (with a 17% PCE) was employed.

Shortly after these first reports, Albrecht et al. reported a 2 T PSTSC using a silicon heterojunction (SHJ) as the bottom cell [38]. In terms of the top cell, citing the SHJ’s low-temperature tolerance, they replace the mesoporous TiO₂ with a planar SnO₂ layer for the ETL. This has added benefit since it allows a planar perovskite deposition. The focus of this work was to fabricate a PSTSC with a SHJ bottom cell, and as such, the perovskite composition is not a main focus, only being briefly referred to in the experimental section, but contains a mix of MA and FA in the A position, and a mix of iodide and bromide in the X position. This cell achieved a PCE of 19.9%, already a substantial improvement on the first 2 T PSTSC, pointing to the merits of both SHJ bottom cells and mixed A ion perovskites.

The previous examples discussed featured cells in a ‘conventional’ n-i-p architecture. This was by far the prevailing architecture for single-junction PSCs [23]. In a single junction PSC, the transparent front electrode can be placed

Fig. 4 **a** Schematic and SEM image of the first reported PSTSC from Mailoa et al., **b** J-V curve of the tandem cell, **c** EQE plot of the two sub-cells combined. Reprinted from Appl. Phys. Lett., 2015, 106, 121,105, with the permission of AIP Publishing



either on top of the HTL or ETL no matter the architecture, however, in a 2 T tandem cell, the ETL in a n-i-p architecture contacts with the silicon bottom cell, and the HTL (almost exclusively spiro-OMeTAD) faces the Sun. Spiro-OMeTAD is well known to cause parasitic absorption, and is unstable at temperatures above 85 °C [39–41]. As such, Bush et al. fabricated a PSTSC in an inverted p-i-n architecture, where the ETL faces the sun instead of the HTL [42]. This device utilised a mix of Cs, FA, I and Br in the lead-based perovskite, with the formula $\text{Cs}_{0.17}\text{FA}_{0.83}\text{Pb}(\text{Br}_{0.17}\text{I}_{0.83})_3$. The HTL was NiO_x , which they noted achieved higher voltage and stability than PEDOT:PSS. The latter was the more commonly employed HTL for p-i-n PSC devices at the time [43]. The ETL comprised of $\text{LiF/PCBM/SnO}_2/\text{ZTO}$. In the following years, research has focused on elucidating the degradation mechanisms of the perovskite, and methods to mitigate this degradation.

6 Halide phase segregation

Halide phase segregation (Fig. 5) has been a known issue with perovskite materials used for solar cells since PSTSCs began to emerge [31, 44].

It was observed that upon illumination, perovskite materials containing a mix of bromide and iodide would segregate and trap states would form, photocarriers would therefore be funnelled to the lower bandgap, iodide-rich phases, reducing the V_{oc} [27, 46, 47]. This effect was especially pronounced when the bromide proportion was greater than 20% of the halide composition [31]. In particular, the ‘soft’ nature of the perovskite lattice facilitates halide migration [48] induced by oxidation of I^- to I_2 in precursor solutions to generate I vacancies [45, 49].

A recent study used time-resolved photoluminescence spectroscopy and transient absorption spectroscopy to indicate that these trap states that cause nonradiative recombination mainly reside at the perovskite/ETL interface (in a p-i-n type cell). These trap states can be suppressed by adding a MgF_2 layer between the perovskite and the C_{60} ETL

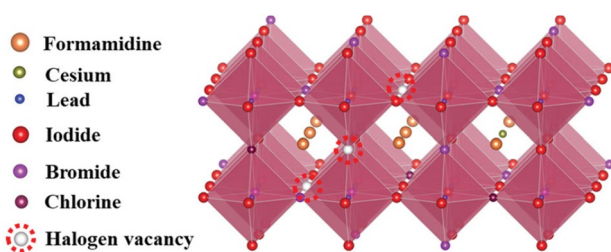


Fig. 5 Depiction of halogen phase segregation creating halogen vacancies. Reprinted from Small 2022, 18 (38), 2,203,319 with the permission of Wiley Publishing [45]

[50]. Another study identified positive iodide interstitials (I_i^+) as the dominant deep charge-trapping defect. Bromide’s smaller size leads to an increase in the concentration of I_i^+ formation upon increased bromide content. This is related to the Pb-Br-Pb angle, which is 13° wider than the Pb-I-Pb angle, leading to increased Br-Br and Br-I distances compared to I-I [51]. This was confirmed by measuring the trap density of states with and without bromide present, which confirmed trap states at 0.12 eV and 0.35 eV. The state at 0.35 eV (I_i^+) increased with increased bromide content, consistent with previous studies [52, 53]. The A cation was previously ruled out as the cause [54]. Crucially, phase segregation more commonly occurs at the grain boundaries, due to localised tensile strain occurring there [55]. As such, methods to passivate phase segregation can include altering the bulk composition of the perovskite, or incorporating additives that remain at the grain boundaries.

7 Tailoring the perovskite to maintain stability

Methods to suppress phase segregation include altering the perovskite composition itself, or by including an additive to prevent halide migration.

Phase segregation is prone to occur with increasing bromide concentration. Therefore, one method is to simply reduce the bromide amount, and increase the bandgap by tailoring the A cation instead. A 2020 review by Zhang et al. compared the PCE of various different A cation configurations (Fig. 6) [56].

MA has been one of the most commonly reported A cations used in perovskite absorbers, however, it is known to be unstable, especially compared to FA [57]. However, attempting to incorporate Br^- into FAPbI_3 in order to sufficiently widen the bandgap for tandem applications also causes instability by causing the formation of an amorphous phase. This reduces the charge-carrier mobility and diffusion length [58]. In line with this, Zhang et al. noted that no mono-cationic FA-based PSTSCs have been reported [56].

The use of Cs^+ as a dopant is commonplace, as it improves structural, thermal and optical stability by inhibiting the transition to the photoinactive yellow perovskite phase. It stabilises the structure [59, 60], while also widening the bandgap [61]. While Cs^+ improves the crystallinity and reduces trap state density, excess Cs^+ can result in poor film morphology and reduced electrical properties due to induced stress [57, 62]. Additionally, excess Cs^+ can also contribute to halide phase segregation [63].

Rb^+ has also been explored for use in perovskites, as it can also stabilise the structure against thermal and optical instability [64], however, it is difficult to incorporate into the lattice, limiting its use to a maximum of 5% [65]. Moreover,

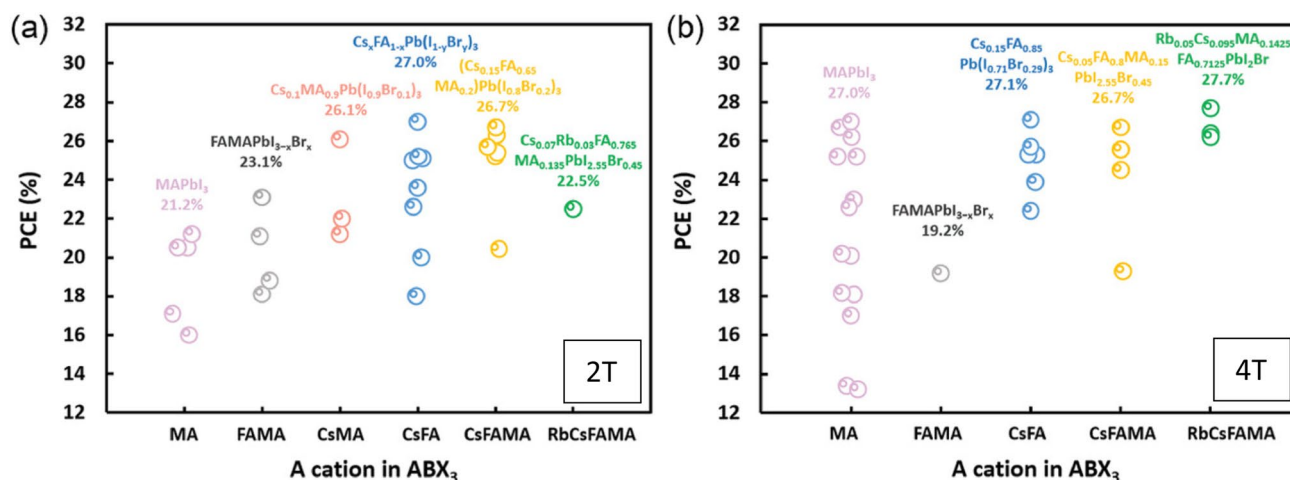


Fig. 6 Reported PCE values versus A cation configuration in **a** 2 T PSTSCs and **b** 4 T PSTSCs. Note that the formulas located at the top of each column refer to the highest reported PCE containing that A cation configuration, and the stoichiometries and X anion com-

position of the other entries may differ (data in tabulated form in Table 1 of ref [56]) Reprinted from Adv. Funct. Mater. 2020, 30 (38), 2,001,904 with the permission of Wiley Publishing

several non-photoactive side products, specifically RbPbX_3 formed during synthesis and $\text{RbPb}_2\text{I}_4\text{Br}$ formed from exposure to humid air, are formed, which reduce light absorption, and reduce the bandgap by extracting Br ions [66].

Tailoring the halide composition is a common technique to adjust the bandgap in PSTSC perovskite layers. However, if the bromide content is above 20%, phase segregation is more likely to occur [46, 47]. The use of chloride in PSTSCs has not garnered much attention until recently (Zhang et al.'s 2020 review collated over fifty PSTSC examples in a table, of which only one contained chloride) [56]. This is perhaps due to the difficulty in incorporating chloride into the perovskite bulk [67, 68], and its minor effect on the bandgap (which is likely related to its poor incorporation) [69]. Nevertheless, chloride has been found to have a stabilising effect on the perovskite [70], and improves crystallinity [67]. A triple halide PSTSC containing Cl^- was fabricated, and the charge-carrier mobility and photocarrier lifetime was improved, and a PCE of 27% was reported [71]. It was found that Cs^+ and Br^- act as a bridge to improve Cl^- solubility by shrinking the lattice parameter, allowing a Cl^- proportion of up to 15%. Overall, the inclusion of Cl^- improves the photostability and optoelectronic properties, paving the way for triple halide perovskites for PSTSCs [72–75].

Other additives (Fig. 7) have been shown to help suppress phase segregation. The same study that identified iodide interstitials as the main defect utilised tribromide ions to suppress this effect [51]. Using trimethyl phenyl-ammonium tribromide (TPABr_3) at a concentration of 0.2 mol% relative to Pb, the trap density was reduced, the V_{oc} was increased and no effect on the morphology or bandgap was observed. Additionally, as the authors fabricated the device on textured

silicon, they required a thicker than usual perovskite layer of 1 μm , in contrast to perovskites deposited on planar silicon which are generally kept below a thickness of 600 nm. While TPABr_3 -free perovskites exhibited lower PCE at thicknesses above 660 nm due to reduced FF and J_{sc} , the inclusion of TPABr_3 showed greater tolerance to increasing thickness, suggesting reduced charge recombination and increased carrier diffusion lengths. A champion PCE of 28.6% and FF of 78.5% was achieved with a 1 μm thick perovskite composed of $\text{Cs}_{0.1}\text{FA}_{0.2}\text{MA}_{0.7}\text{Pb}(\text{I}_{0.85}\text{Br}_{0.15})_3$, with 0.2 mol% TPABr_3 on a textured SHJ bottom cell.

The issue of I^- oxidation to I_2 in the precursor solution can be mitigated with the addition of benzylhydrazine hydrochloride (BHC) (0.83 mg ml^{-1} in a 1.37 M solution), and, furthermore, residual BHC was found to improve the perovskite stability in single-junction p-i-n type PSCs [49]. Alternatively, ammonium diethyldithiocarbamate (ADDC) can be used for this reduction process, and when employed in a 4 T PSTSC, a PCE of 30.24% was achieved [45]. In both of these cases, the cells retained >90% of their initial efficiency after 500 h.

Pointing to the stabilizing effect of ionic additives in single junction PSCs (namely theophylline [76], imidazolium [77] and piperidinium [78]), particularly at grain boundaries where a significant amount of charged defects occur, Liu et al. utilised carbazole derivatives to passivate deep charge traps, enhance performance and suppress phase segregation [79]. This was achieved via interaction with the halides through H-bonds, specifically at the grain boundaries as the carbazole molecules are too large to be incorporated into the bulk. A PCE of 28.2% was achieved, and after a 43-day outdoor test in hot and dry conditions, 93%

of the original PCE was maintained. We highlight that a number of high efficiency p-i-n type PSTSCs use a carbazole-derived self-assembling monolayer (SAM) as the HTL, specifically Me-4PACz (achieving 29.15% PCE with a $\text{Cs}_{0.05}(\text{FA}_{0.77}\text{MA}_{0.23})_{0.95}\text{Pb}(\text{I}_{0.77}\text{Br}_{0.23})_3$ perovskite) [80], and 2PACz (27.9% PCE with an optimised Si bottom cell) [81]. In Table 1 devices containing a SAM with even higher PCE can be found.

2D perovskites (Fig. 8) represent another method to passivate the grain boundaries. By using a variety of ammonium cations, researchers have generated 2D perovskite layers at the grain boundaries of 3D perovskite crystals, which has been shown to passivate defects. While molecules such as butylammonium(BA) [83, 84] and thiophene derivatives (including thiophene-methylammonium (TMA) [85] and thiophene-ethylammonium(TEA) [85, 86] have been used

Table 1 Recently reported PSTSCs sorted by PCE. Clearly, the rise in efficiency is mainly controlled by a rise in voltage, indicating improved carrier management

PCE (%)	Perovskite Composition	Band gap (eV)	Si cell	Chemicals used and Additives	V_{oc} (V)	J_{sc} (mA cm^{-2})	FF (%)	Year	Refs
33.9					1.966	20.76	83.0	2023	[6]
33.7					1.974	<u>20.99</u>	81.3	2023	[6]
33.2					1.962	20.97	80.7	2023	[6]
32.5	$\text{Cs}_{0.05}\text{FA}_{0.8}\text{MA}_{0.15}\text{Pb}(\text{I}_{0.755}\text{Br}_{0.255})_3$	1.68	(2 T) SHJ, n-text	2PACz	1.948	20.90	79.8	2023	[92]
32.5	$\text{Cs}_x\text{FA}_{1-x}\text{Pb}(\text{I}_y\text{Br}_z\text{Cl}_{1-y-z})_3$	1.68	(2 T) SHJ, text. (b)	Me-4PACz, PI	<u>1.980</u>	20.24	81.2	2022	[75] [91]
31.3	$\text{Cs}_{0.18}\text{FA}_{0.82}\text{Pb}(\text{I}_x\text{Br}_{1-x})_3$	1.70	(2 T) SHJ, text	Me-4PACz, FBPAc	1.91	20.47	79.8	2022	[93] [91]
30.3	$\text{Cs}_{0.1}\text{FA}_{0.9}\text{Pb}(\text{I}_{0.9}\text{Cl}_{0.1})_3$	1.55	(4 T) SHJ, text	4-MPEACl				2023	[89]
30.24	$\text{Cs}_x\text{FA}_{1-x}\text{Pb}(\text{I}_y\text{Br}_z\text{Cl}_{1-y-z})_3$	1.77	(4 T) SHJ, text	ADDC				2022	[45]
29.8	$\text{Cs}_{0.05}(\text{FA}_{0.79}\text{MA}_{0.21})_{0.95}\text{Pb}(\text{I}_{0.79}\text{Br}_{0.21})_3$	1.66	(2 T) SHJ n-text		1.92	19.56	79.4	2022	[6, 94]
29.5					1.884	20.26	77.3	2021	[91]
29.15	$\text{Cs}_{0.05}(\text{FA}_{0.77}\text{MA}_{0.23})_{0.95}\text{Pb}(\text{I}_{0.77}\text{Br}_{0.23})_3$	1.68	SHJ, pol	Me-4PACz	1.90	19.23	79.4	2020	[6, 80]
28.7	$\text{Cs}_{0.22}\text{FA}_{0.78}\text{Pb}(\text{I}_{0.85}\text{Br}_{0.15})_3$	1.68	TOPCon PERC	2PACz, PI, MACl, PbCl_2	1.904	19.49	78.3	2022	[95]
28.6	$\text{Cs}_{0.1}\text{FA}_{0.2}\text{MA}_{0.7}\text{Pb}(\text{I}_{0.85}\text{Br}_{0.15})_3$	1.65	SHJ, text	TPABr_3 0.2 mol%	1.92	19.00	78.5	2022	[51]
28.6	$\text{Cs}_x\text{FA}_{1-x}\text{Pb}(\text{I}_y\text{Br}_{1-y})_3$	1.68	SHJ, text	MA ($\text{Cl}_{0.5}\text{SCN}_{0.5}$)	1.85	19.80	78.9	2023	[96]
28.51	$\text{Cs}_{0.1}\text{FA}_{0.9}\text{PbI}_{2.74}\text{Br}_{0.16}\text{Cl}_{0.1}$	1.626	SHJ, text	TEABr	1.849	19.35	79.6	2022	[86]
28.2	$\text{Cs}_{0.05}\text{FA}_{0.8}\text{MA}_{0.15}\text{Pb}(\text{I}_{0.75}\text{Br}_{0.25})_3$	1.68	SHJ, text	2PACz	1.865	19.60	78.4	2021	[79]
27.9	$\text{Cs}_{0.05}(\text{FA}_{0.77}\text{MA}_{0.23})_{0.95}\text{Pb}(\text{Br}_{0.23}\text{I}_{0.77})_3$	1.68	SHJ, pol	2PACz	1.92	17.80	80.9	2021	[81]
27.2	$\text{FA}_{0.83}\text{MA}_{0.17}(\text{PbI}_3)_{0.83}(\text{PbBr}_3)_{0.17}$		SHJ, pol		1.819	18.10	<u>82.4</u>	2023	[97]
27.04	$\text{Cs}_{0.22}(\text{FA}_x\text{MA}_{1-x})\text{Pb}(\text{Br}_{0.15}\text{I}_{0.82}\text{Cl}_{0.03})_3$	1.67	SHJ, pol		1.886	19.12	75.3	2020	[71]
26.7	$\text{Cs}_{0.15}\text{FA}_{0.65}\text{MA}_{0.2}\text{Pb}(\text{I}_{0.8}\text{Br}_{0.2})_3$		SHJ, pol	PEA ($\text{I}_{0.25}\text{SCN}_{0.75}$)	1.756	19.20	79.2	2020	[87]
25.7	$\text{Cs}_{0.05}\text{FA}_{0.8}\text{MA}_{0.15}\text{Pb}(\text{I}_{0.75}\text{Br}_{0.25})_3$	1.68	SHJ, text	1-butane-thiol	1.787	15.88	74.5	2020	[98]
25.1	$\text{Cs}_x\text{FA}_{1-x}\text{Pb}(\text{I}_y\text{Br}_{1-y})_3$		PERC, text		1.738	19.50	74.1	2019	[99]

Chloride components appear important for highest 30+ % PCE. Italic values are derived. Combining the highest values (underlined) gives a projected 34.5% PCE. “text.” is textured, “pol.” is polished, n-text. is nano-textured. (b) implies texturing of the back of the cell only. PI = piperazinium iodide. Me-4PACz = [4-(3,6-Dimethyl-9H-carbazol-9-yl)butyl]phosphonic Acid. FBPAc = 2,3,4,5,6-pentafluorobenzylphosphonic acid. 2PACz = (2-(9H-carbazol-9-yl)ethyl)phosphonic acid. See also Figs. 7 and 13 for structures

for single junction PSCs and PSTSCs, phenethylammonium (PEA) derivatives have emerged as the front-runners for PSTSC use [87–89].

The use of TEA-Br in a PSTSC on textured c-Si and using a $\text{Cs}_{0.1}\text{FA}_{0.9}\text{PbI}_{2.74}\text{Br}_{0.16}\text{Cl}_{0.1}$ perovskite was shown to improve the V_{oc} by 100 mV compared to a control without TEA-Br, and a PCE of 28.51% was achieved with no significant decay occurring after 500 h of 1-sun illumination under encapsulation. Scaling this cell up from 0.5 to 11.9 cm^2 retains an efficiency of 25.13% [86]. The use of BA^+ was examined in a 4 T PSTSC using IBC c-Si and a $\text{Rb}_{0.05}\text{Cs}_{0.095}\text{MA}_{0.1425}\text{FA}_{0.7125}\text{PbI}_2\text{Br}$ perovskite to achieve a PCE of 27.7%. However, this featured a 2D perovskite at the surface, giving a negative effect on grain size and crystallinity when incorporating into the bulk [84].

Unlike BA^+ , the inclusion of PEA-I resulted in improved crystallinity as concentration increased towards 10 mol% in a $(\text{FAPbI}_3)_{0.85}(\text{MAPbBr}_3)_{0.15}$ perovskite single-junction PSC. In this case, the PCE, J_{sc} and FF decreased due to the insulating nature of PEA^+ [90]. Nevertheless, V_{oc} increased, and greater stability was observed compared to a control device. PEA^+ was later incorporated into perovskites for PSTSCs, but this time incorporating mixed SCN^- and I^- anions. With greater electrical conductivity due to the presence of SCN^- , the J_{sc} and FF were improved, and ultimately a PCE of 26.7% was reported for a $(\text{FA}_{0.65}\text{MA}_{0.2}\text{Cs}_{0.15})\text{Pb}(\text{I}_{0.8}\text{Br}_{0.2})_3$ perovskite in a 2 T tandem cell. The PEA^+ composition was optimised to $\text{PEAI}_{0.25}\text{SCN}_{0.75}$ [87].

2 mol% 4-methyl-PEACl was found to form quasi-2D perovskite layers at the grain boundaries of an MA-free perovskite. The 4-MPEACl additive was found to enhance hole extraction at the surface of the perovskite, and promote homogeneous nucleation leading to larger crystal grains. As the $\text{FAPbI}_3/\text{CsCl}$ -based perovskite has a relatively low bandgap for a PSTSC top cell of 1.55 eV, a 4 T configuration was used, which is much less sensitive to varying bandgap compared to the 2 T configuration (Fig. 3), and a PCE of 30.3% was achieved, of which 98% was retained after a 42 day/night cycle stability test [89].

8 Tailoring the perovskite towards higher power conversion efficiency

Table 1 compiles a number of recently reported high PCE PSTSCs. These include those discussed so far in this work, as well as some of the recent records reported by NREL. A number of these are missing key data points, in particular, some of the recently certified record-holders have not disclosed their compositions, and only the PCE, V_{oc} and FF have been reported on the NREL website [91]. Other reports have not disclosed the exact compositions of their perovskites, only mentioning the ions contained within. In these

cases, the focus of the research was on other components of the PSTSC, such as the bottom cell, the CTLs or the effect of an additive.

The data in Table 1 indicates that a textured SHJ bottom cell, combined with a perovskite material containing 5 to 15% Cs, no MA, only FA, and iodide together with a substantial amount of chloride leads to the best TSCs. An amount of bromide (up to 20%) can then be used to tune the bandgap towards to optimal 1.73 eV. It should be noted that “Perovskite Composition” in Table 1 reports (mainly) the composition of the precursor solutions used. The exact composition of the perovskite thin solid film is rarely determined and can strongly deviate from the precursor solution composition. Considering the data in Table 1, we do not anticipate that single halide perovskites [100] nor all inorganic perovskites [101] will play a dominant role in this field.

9 Composition of the bottom silicon cell

The two main categories of c-Si solar cells (Fig. 9) are homojunction solar cells, which utilise only c-Si as the semiconducting material, only with different dopants, and heterojunction solar cells, which utilise hydrogenated amorphous silicon (a-Si:H) as a buffer/passivation layer [102]. In recent years, passivated emitter rear cells (PERC), a type of homojunction solar cell, have led the increase in PCE of single junction c-Si solar cells [103–105], and are expected to have a market share of > 70% by 2030 [106]. Alternatively, silicon heterojunction (SHJ) cells make up a smaller market share of 15% [106], however, according to a 2022 review, the majority of reported PSTSCs with a PCE greater than 25% have employed an n-type SHJ as the bottom cell [32].

Fu et al.’s 2022 review provided a comprehensive overview of the types of Si used thus far [32]. The advantage of PERC cells lie in their market dominance as single-junction cells, and their higher temperature tolerance which allows for the sintering of efficient ETLs such as TiO_2 and SnO_2 . [107, 108]. Despite this, adaptations are needed to facilitate use in PSTSCs. In particular, the dielectric $\text{SiN}_x/\text{AlO}_x$ layer for surface passivation/antireflection is insulating in nature, and must be either replaced with a TCO, which causes a drop in V_{oc} . [109, 110] or openings in this layer can be created using photolithography followed by deposition of a conductive material [108]. Utilising this method in a PSTSC resulted in a PCE of 22.5% (in 2017). These prior examples used n-type PERC substrates, but p-type substrates can also be used. In 2019, a p-type cell, with front texturing, was reported with a SiO_x and phosphorus-doped $\text{SiC}_x(\text{n})$ front contact, with a p-type nanocrystalline nc-Si(p):H as a recombination junction with the perovskite. This configuration, together with an unspecified p-i-n type perovskite layer, achieved a PCE of 25.1%, which represented a 2.5% increase

from the PCE of the same silicon cell as a single-junction device [32, 99]. In 2022 a PCE of 28.7% was reported with a PERC bottom cell [95]. This improvement is mainly due to a 170 mV increase in the V_{oc} , indicating better charge management. A small FF increase can also be noted (from ~ 0.74 to ~ 0.77). The use of a SAM composed of 2PACz and PI as ETL are hereby identified as an important aspects of this improvement.

Many high-efficiency PSTSC's with a PCE above 25.1% have been fabricated using SHJ bottom cells. These cells contain typically n-type c-Si passivated by intrinsic doping and p-doped a-Si:H on the surface. As a single junction cell, they utilise a TCO with Ag metal as electrodes, which can be adapted to form a recombination junction. They exhibit higher V_{oc} compared to PERCs [111], and excellent NIR absorption [112], but suffer from a low-temperature coefficient (temperature resilience), limiting the fabrication to low-temperature perovskite deposition processes, caused by H effusing out of the a-Si:H, losing passivation and restricting the ability to withstand high temperatures above 250 °C [113]. SHJ's lack in popularity compared to PERCs, as a single-junction cell, is due to their lower photocurrent caused by parasitic absorption of blue light by the a-Si:H and the TCO, but this is not an issue with PSTSCs as the perovskite top cell now absorbs this part of the spectrum [114].

TOPCon-technology [115] based on high-temperature passivating contacts (HTPC) can produce 4 cm² tandem devices with 28.25% PCE. TOPCon stands for tunnel oxide-passivating contact and is also used by Q-cells/Hanwha in Si technology.

The actual c-Si wafer is typically one of two kinds: 'float-zone' (FZ) or 'Czochralski' (Cz), reflecting the type of process used in manufacturing. FZ Si is purer, higher quality silicon, but its production method limits wafer size to around 150 mm, while Cz Si is of lower quality, but can be made to larger wafer sizes and is cheaper [116]. As researchers tend to aim for higher efficiencies, higher-quality FZ Si tends to be more frequently used. However, a 2021 study comparing the two types in PSTSCs found a PCE difference of only 0.26% between 100 μm Cz and 280 μm FZ bottom cells, indicating that Cz Si is viable for use in industry [81].

10 Texturing silicon

Texturing of silicon solar cells (Fig. 10) is standard practice in the industry to improve light trapping, but the majority of PSTSCs have been produced on flat, polished silicon surfaces. This is due to the difficulties in depositing the perovskite by a solution process (primarily spin coating) onto a textured surface [73]. The first successful example produced in 2018 achieved a 25.2% PCE, and the top cell was deposited on the textured Si by a two-step method, wherein PbI_2

and CsBr are co-evaporated onto the Si bottom cell (with the HTL thermally evaporated) followed by spin-coating of FABr and FAI [117].

The previous example utilised textured pyramid sizes of around 5 μm , similar to the industry standard for single-junction Si cells. However, this was achieved with a top cell comprising only the basic perovskite precursors. Additives are normally incorporated to aid stability and performance. This process thereby becomes more complex and difficult to achieve a conformal coating. However, solution processing on fully textured SHJ cells aided by 1-butanethiol can give 25.7% PCE perovskite on silicon tandem cells [98].

As such, further research in this area looked towards more mildly textured Si, with pyramid sizes ranging around 1 μm . For example, Chen et al. developed a blade coating process to deposit a perovskite top cell onto a Si bottom cell with sub-micron texturing [118]. Unlike the previous thermal evaporation method, this method retains the benefits of a solution-based process while also ensuring complete coverage of the Si pyramids and allowing the use of additives. A PCE of 26% was achieved.

More recently, a study was conducted on the effects of Si texturing on the structural and optoelectronic properties of the perovskite top cell [119]. Spin-coating was applied as a deposition method. It was found that the main impact of texturing lied in the photoluminescence (PL) spectra, which showed a shift from 1.67 eV of the $\text{Cs}_{0.05}\text{MA}_{0.14}\text{FA}_{0.81}\text{Pb}(\text{I}_{0.8}\text{Br}_{0.2})_3$ perovskite on flat Si, to 1.65 eV on textured Si. This implies that a less optimal perovskite bandgap is obtained on a texture Si surface for an identical perovskite composition. The effects of temperature and halide distribution were ruled out, and the thickness of the perovskite was found to be the main contributing factor, with a test carried out with 250 and 900 nm thick perovskites on flat Si showing a similar PL shift. As previously mentioned in this work, the carrier diffusion length can be increased and the perovskite's tolerance to thickness can be improved by the use of a TPABr₃ additive [51]. Clearly, compatibility of the Si surface (flat vs textured) with the perovskite deposition method is essential for industrial applications. In this regard, co-evaporation methods are promising [120, 121].

The addition of anionic additives, specifically Cl^- and SCN^- was found to improve the crystallisation of the perovskite on textured Si, reducing the trap density and aiding in achieving conformal deposition [96]. A 50:50 ratio of MA₂Cl and MA₂SCN added to the FAI/FABr precursor solution was found to perform best, with too much SCN leaving the Si pyramid tips exposed, and too much Cl not having a noticeable effect (Fig. 11). The addition of the anions enabled larger grain sizes and suppressed light-induced halide segregation by reducing trap densities, achieving a PCE of 28.6%. Moreover, this technique was shown to be scalable,

with a 16 cm² device exhibiting a PCE of 25.1%, and in both cases, encapsulation retains 80% of the efficiency after 2000 h. It is worth noting that MA was not included in the control sample, only FA was used.

A reflector with a dielectric buffer layer, comprising of SiO₂, located at the rear of the bottom cell between the TCO and the Ag electrode can be utilised together with a nanotextured front side with a sinusoidal nanostructure with 300 nm dimensions. This achieved a PCE of 29.8%, which was record-breaking at the time. As the addition of the reflector increased the current density of the bottom cell, to maintain current matching conditions, the bandgap of the perovskite was shifted from 1.68 eV to 1.66 eV, which was achieved by reducing the amount of bromide and increasing the amount of FA (from a composition of (Cs_{0.05}(FA_{0.77}MA_{0.23})_{0.95}Pb(I_{0.77}Br_{0.23})₃ to Cs_{0.05}(FA_{0.79}MA_{0.21})_{0.95}Pb(I_{0.79}Br_{0.21})₃) [94].

All aspects considered the concept arises that a flat interface between Si and perovskite (with a textured Si backside) is more advantageous than texturing on both Si sides. Especially if SAM formation on the thin (ITO) interface layer is an important aspect of the design, this makes sense, since self-assembled mono-layers form more compact, organized and homogeneous layers on (atomically flat) surfaces. However, optimization of the texturing of tandem cells is still needed, by for instance comparing different options in one experimental test (keeping all other factors constant and taking into account the cost factors). The deposition method is also an essential aspect of this factor, as well as the type of structuring (micro- or nano-structuring). Important options can be defined: i) only flat surfaces, ii) only flat interface, iii) textured silicon but flat perovskite surface (e.g. when blade- or spin-coating is applied) and iv) textured silicon and textured perovskite (with conformal perovskite deposition by using co-evaporation or hybrid deposition). It can be noted that the 32.5% PCE device (see also Table 1) incorporates only a textured back.

Nano-texturing both sides of the silicon by using etching procedures not only containing KOH but also K₂SiO₃ has been reported [122] and can induce sub-micrometer features (~ 500 nm).

11 Interface layer between silicon and perovskite

In a 2 T PSTSC, the two sub-cells must be connected monolithically, typically requiring the use of a tunnel junction (TJ) or recombination layer (RL) as an interface. This layer requires high optical transparency, and good out-of-plane conductivity for efficient hole and electron transport and low voltage loss while having low in-plane transport to prevent shunting channels. Typically, this layer is a TCO, such as

ITO [98] or ZTO [110] with a thickness below 20 nm to reduce shunting channels and optical losses [71]. However, other materials such as a-Si [42], nc-Si [123] or nc-SiO_x [124] have also been reported. An example of a PSTSC with homojunction Si without the need for an additional interface also exists. It utilises the intrinsic interface between the SnO₂ ETL of the top cell with the p + + emitter of the bottom cell [125].

As the interface becomes thinner, less parasitic absorption occurs, and trap states for carrier recombination are reduced. As such, Zheng et al. reported an ultra-thin ITO interlayer with a thickness of 1.7 nm (Fig. 12) [97]. While achieving a PCE of 27.2% PCE, the FF of 82.4% is the highest of a PSTSC reported to date. Moreover, this was shown to be scalable, with cells of sizes 11.8 cm² and 65.1 cm² fabricated, exhibiting PCEs of 24.2% and 21.1% respectively.

As discussed earlier, the ITO interface layer can be functionalized with a self-assembled monolayer (SAM) using phosphonic acid derivatives (see also Table 1). Especially carbazole derivatives are suitable for this purpose, which act as a hole transport layer (HTL). Me-4PACz has been applied in various tandem devices, combined with other active components such as ionic liquid PI^[175] (as an extra electron transport layer, ETL, with electron donor–acceptor character) and combined with FBPAc [93] (influencing crystal growth). The molecular structures of these active components of high-efficiency tandem devices are given in Fig. 13.

Clearly, phosphonic acids and ionic liquids are excellent candidates for ultra-thin functional layers in tandem cells. Whereas chain length optimization has been obtained for Me-4PACz, further carbazole functionalization as well as exchanging the counter ion of PI for (I₃)⁻ or (Br₃)⁻ present further avenues to explore.

Substituted carbazole derivatives containing carboxylic acid groups as well as phenothiazine systems with phosphonic acid tails incorporated directly in the perovskite precursor solution have been shown to lead to surface functionalization of ITO [126]. SAM formation and perovskite deposition can be accomplished in one procedure.

To clarify the use of these organic molecules as active components in perovskite-silicon tandem solar cells, the stack structure of the 32.5% PCE device is schematically represented in Fig. 14. Additional information on (optimized) layer thickness, properties and function is inserted. It can be noted that PI layer thickness is not specified (but the concentration of solution for spin coating is). The perovskite layer thickness is an estimate extracted from the supporting information of ref [75].

Current matching of both sub-cells at the maximum power point of the tandem can be approximated by the matching of their short circuit currents if individual fill-factors are identical. For optimal performance, equal amounts

of positive charge carriers from the top cell and negative charge carriers from the bottom cell (or vice versa) should arrive at the recombination layer (per time unit). Identical fill-factors indicate equal charge loss and thus current matching implies absorption of equal amounts of photons for the two sub-cells [127, 128].

The multi-layered stack structure can be used to exemplify the function of the recombination layer (RL): positive charge carriers (holes) photo-generated within the perovskite layer have to transport to the RL (through the HTL) and recombine with an equal amount of negative charge carriers (electrons) photo-generated in the Si layer, thereby enhancing the output voltage at current matching conditions. Negative charge carriers (electrons) photo-generated in the perovskite layer will move (through the ETL) to the top contact. Positive charge carriers (holes) photo-generated within the Si layer will move to the bottom contact.

High-efficiency devices (32.5% PCE) can also be obtained by using an alternative recombination layer of 5 nm thin IZO covered by a SAM of 2PACz as a hole transport layer [92].

12 Discussion and conclusion

PSTSC technology has made astounding progress in only a few years, with record PCEs surpassing the practical limit for single-junction Si cells and expected to rise even further (Table 1). This progress has been achieved primarily through optimisation of the perovskite top cell, with key challenges such as light-induced halide phase segregation being identified and addressed. The tandem field benefits from the perovskite single junction solar cell research. Recent single junction work on alkylammonium additives (25.73% PCE with propylammonium chloride, PACl) [129] and a zinc(II)-based interface layer (23.25% PCE) [130] may bring the field even further, providing an interesting link to earlier work [131–133] performed in Amsterdam that focussed on CPACl (chloropropylammonium chloride) and Zn(II) doping. Synergy between such additives can lead to fine-tuning of the power conversion efficiency.

Composition In terms of the perovskite composition, it has been tuned to include multiple cations and anions to not only tailor the bandgap but to also improve stability. For the A cation, reducing the MA amount has been shown to improve stability, while doping with small amounts of Cs⁺ (below 15%) has also been shown to improve stability and widen the bandgap. Rb⁺ has also been tested as a dopant, but cannot be used above 5% as it causes stability issues. Relatively few reports utilise Rb⁺, and the highest PCE PSTSCs omit the element.

To date, no suitable replacement for Pb has been found for use in top cells. Sn has been reported for single-junction PSCs and as a bottom cell for all-perovskite TSCs. As

Sn reduces the bandgap significantly below 1.5 eV, it is not suitable for use as a top cell in TSCs.

A mix of halides has been found to work best for the X anion, in particular using Br⁻ to widen the bandgap, and also Cl⁻ to aid stability. In order to combat light induced halide phase segregation, the Br⁻ content should be limited to below 20%, although higher content has been reported using stabilisation strategies to suppress phase segregation. Cl⁻ solubility has been an issue, however concentrations up to 15% have been reported to be incorporated into the perovskite when used in combination with Br⁻ and Cs cations.

Additives The use of additives that are not incorporated in the bulk has been found to further aid the stability of the perovskite. In particular, the formation of 2D perovskites by using alkyl-ammonium cations has shown promise in suppressing phase segregation at the grain boundaries. Furthermore, PEA has shown great promise in this area, but more research is required to optimise both the amount, and also the substituents on the phenyl ring (which should be electron-donating in nature). Other additives can be utilised to prevent iodide vacancies, including (Br₃)⁻ (which can also allow for thicker perovskite layers needed for deposition on textured silicon) and reducing agents such as BHC and ADDC to reduce I₂ to I⁻. Note that (I₃)⁻ as well as formate anions (Fo⁻, see Fig. 7) have been shown to optimize single junction devices leading to 22⁺ and 25⁺ % PCE devices, respectively [134, 135].

Bottom cell As for the silicon bottom cell, SHJ is certainly the preferred type over homojunction cells, with all high-efficiency PSTSCs being fabricated with SHJ bottom cells [136]. In terms of optimizing the bottom cell, the only main challenge is to fabricate a PSTSC with industrially textured Si with pyramid sizes greater than 1 μm, while still allowing for solution-processed perovskite deposition. Nevertheless, results from mildly textured Si are promising.

Future In terms of future research, a comprehensive analysis of the perovskite composition should be performed, with all other cell components being kept consistent. While reviews have been conducted on cell composition, in many cases, these feature examples from across the literature and feature differences in other components, such as the CTLs, TCOs or Si bottom cell. As such, it would be beneficial to design a device where the other components are fixed, and the effect of altering the perovskite composition can be independently examined. These experiments could include varying the Cs⁺ doping to find the optimum, optimising the FA:MA ratio or even total elimination of MA. Also, probing the effects of adding Cl⁻ and optimising its ratio compared to the other halides, and the effect of adding multiple additives. For example, adding both PEA molecules for 2D perovskite formation and (Br₃)⁻ for phase segregation suppression and enhanced tolerance to thickness.

Fig. 7 Molecular structures of some constituents and additives featuring in this treatise. Shown are: methylammonium (MA⁺), formamidinium (FA⁺); cationic additives: propylammonium (PA⁺), butylammonium (BA⁺), phenethylammonium (PEA⁺), 4-methyl-phenethylammonium (MPEA⁺), thiopheneethylammonium (TEA⁺), trimethylphenylammonium (TPA⁺), benzyldiazinium (BH⁺); anionic additives: tribromide (Br₃)⁻, triiodide (I₃)⁻, thiocyanate (SCN⁻), diethyldithiocarbamate (DDC⁻), formate = Fo⁻ = (HCO₂)⁻

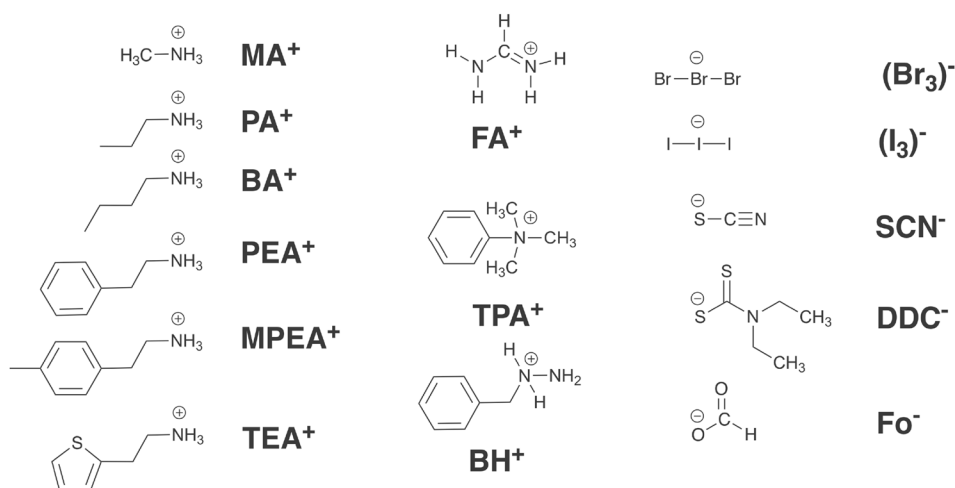


Fig. 8 **a** Diagram showing 2D perovskites forming at the 3D perovskite grain boundaries, **b** illustration of 3D perovskite and 2D perovskite separation induced by *n*-butylamine and **c** by *n*-butylammonium iodide. Reprinted with permission from *J. Phys. Chem. Lett.* 2018, 9 (3), 654–658 Copyright 2018 American Chemical Society [82]

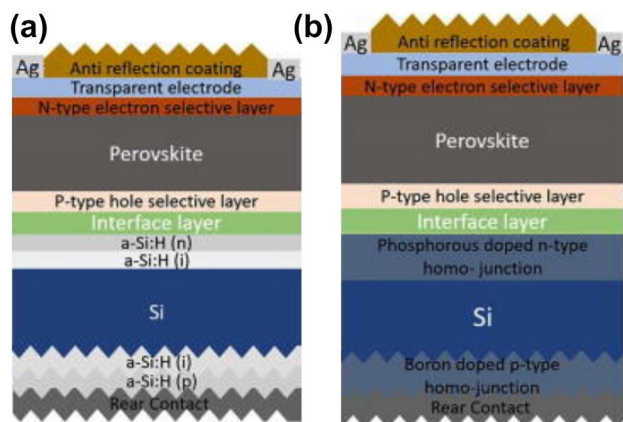
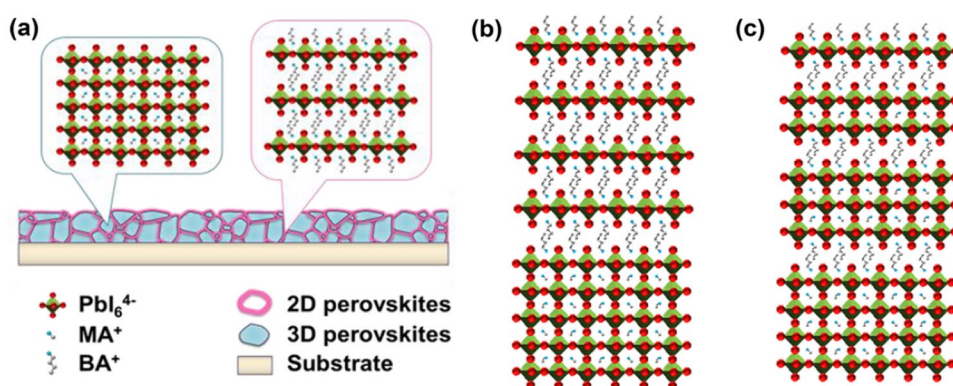


Fig. 9 Comparison between p-i-n type PSTSCs using **a**) SHJ and **b**) homojunction Si as the bottom cells. Reprinted from *Appl. Phys. Rev.* 2021, 8 (4), 041307, with the permission of AIP Publishing [23]

For such an experiment, SHJ is an obvious choice for the bottom cell. For the top cell, a p-i-n architecture has shown greater promise and would be a good choice to build upon, with a Me-4PACz HTL and a PI/C₆₀/SnO₂ ETL, as together

these components have contributed to passing the 30% PCE boundary [94]. As for the perovskite composition, a double or triple mixed cation with double or triple halide has shown great promise. The MA content should be minimized (similar to the development in the single junction field) as MA has been shown to cause instability. The MA content should be less than 25%, lower seems better. Cs⁺ doping should be limited to a maximum of 15%. As for the halide ratio, the bromide should be kept below 20%, even if phase segregation-suppressing additives are used. The incorporation of chloride has proven difficult and has been limited to a maximum of 15%. In a broader context, optimization of the perovskite composition combined with integration into the Si solar wafer production process (with flat or textured surface) with an optimal (atom efficient) perovskite deposition method will be crucial for the realization of tandem products.

There is a strong advancement in understanding the stability issues of the perovskite top cell, in particular light-induced phase segregation (as well as of the optimized PCE). Research continues to elucidate the causes of this phenomenon, and a number of promising solutions

Fig. 10 **a** Schematic representation of SHJ tandem cell. **b** SEM images of a bifacially textured silicon bottom cell with a perovskite cell deposited on top. **c** I/V curves of PSTSC cell with picture of cell and PCE values. **d** EQE spectra of PSTSC with double-side textured silicon together with 1-R plots showing reflection losses. Note the matching currents. Reprinted from *Adv. Mater.*, 2023, 35, 2,207,883, with the permission of Wiley Publishing [96]

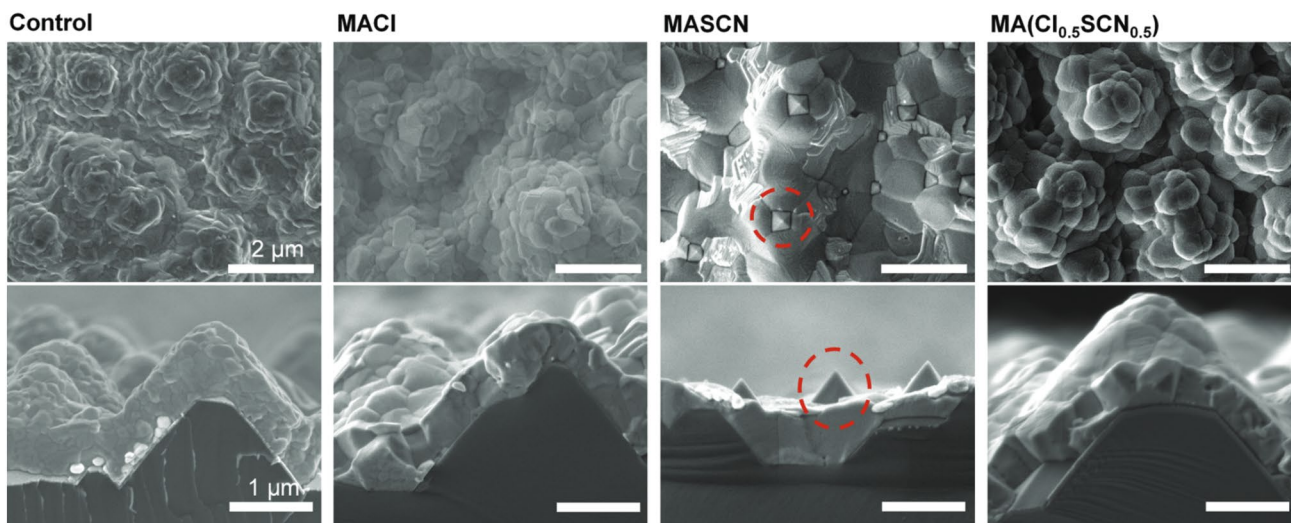
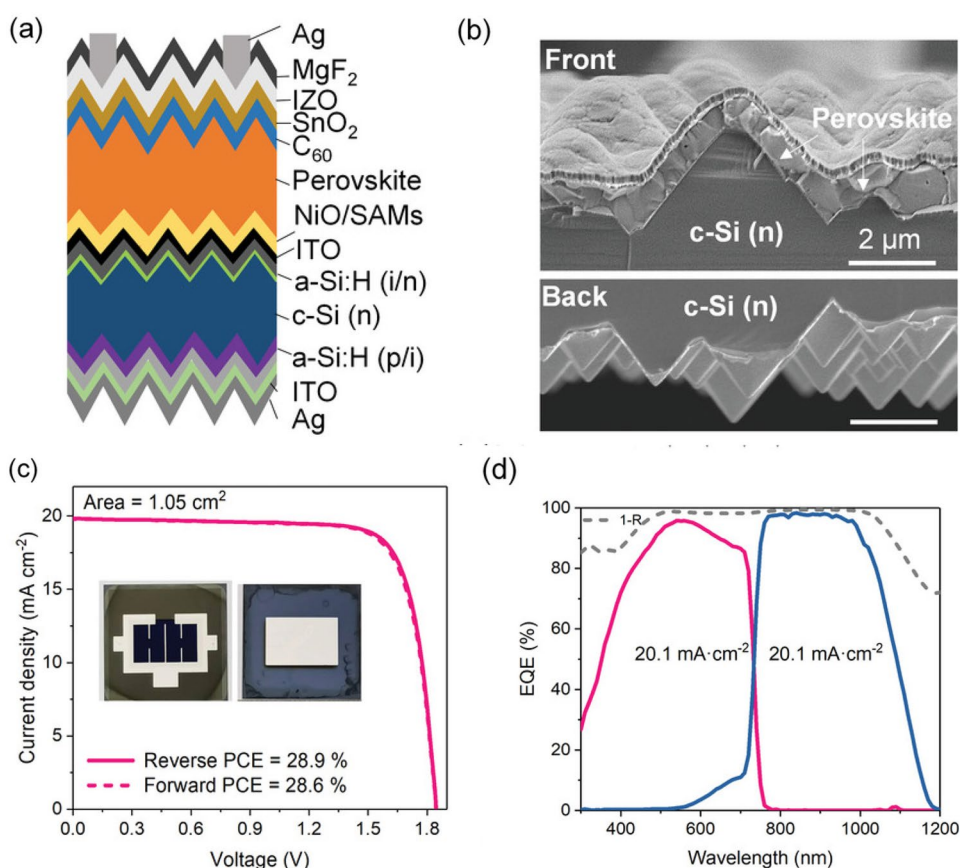


Fig. 11 SEM images of perovskites on textured Si with varying Cl^- and SCN^- additives. Note that as SCN^- concentration increases, the grain size becomes larger, and that when 100% SCN^- is used, the

perovskite does not completely cover the Si tips. Reprinted from *Adv. Mater.*, 2023, 35, 2,207,883, with the permission of Wiley Publishing [96]

to suppress this effect have been presented. The SHJ bottom cell has emerged as the choice material owing to its high V_{oc} and NIR absorption. Efforts to scale up the size of PSTSCs have been promising, with cells larger than

10 cm^2 being developed with efficiencies approaching and surpassing the PCE of single junction c-Si cells. For small tandem cells in the research field, a PCE of 34.5% appears to be within reach (see Table 1). The future is bright, for

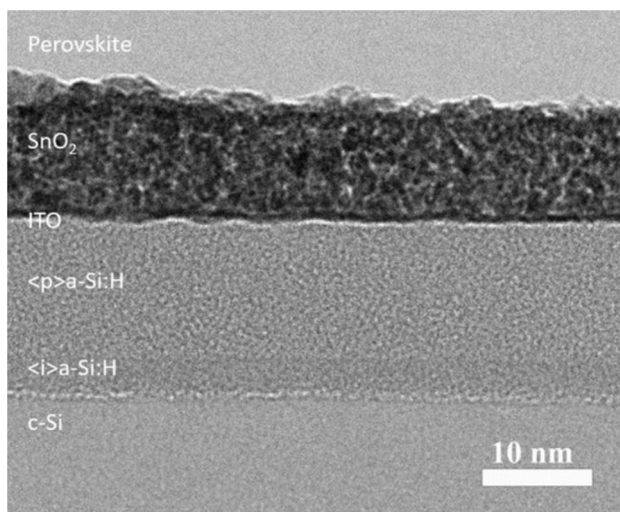


Fig. 12 Bright Field TEM image of a PSTSC featuring an ultrathin ITO interface. Reproduced from *Energy Environ. Sci.*, 2023, 10.1039. D2EE04007G, with permission from the Royal Society of Chemistry [97]

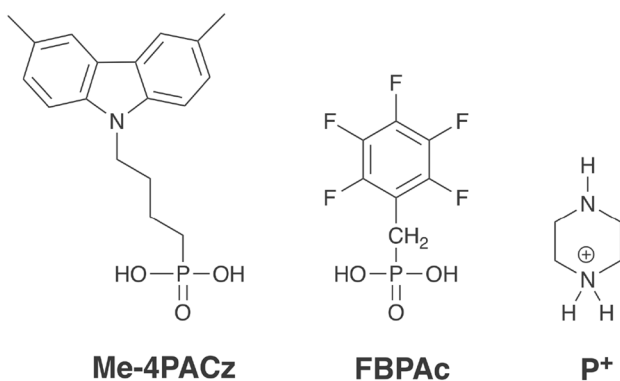


Fig. 13 Molecular structures of active components used in tandem cells. Me-4PACz = [4-(3,6-Dimethyl-9H-carbazol-9-yl)butyl]phosphonic Acid. FBPAc = 2,3,4,5,6-pentafluorobenzylphosphonic acid, P⁺ = piperazinium (used as iodide salt PI). (See also Table 1)

silicon tandem solar cells, with perovskite. Especially when different additives can operate in a synergistic mode of action [137].

Acknowledgements We thank Jordan P. Mulvaney for language corrections, Srest Somay for his help with the graphical abstract and the University of Amsterdam for structural support.

Declarations

Conflict of interest There are no conflicts of interest to declare.

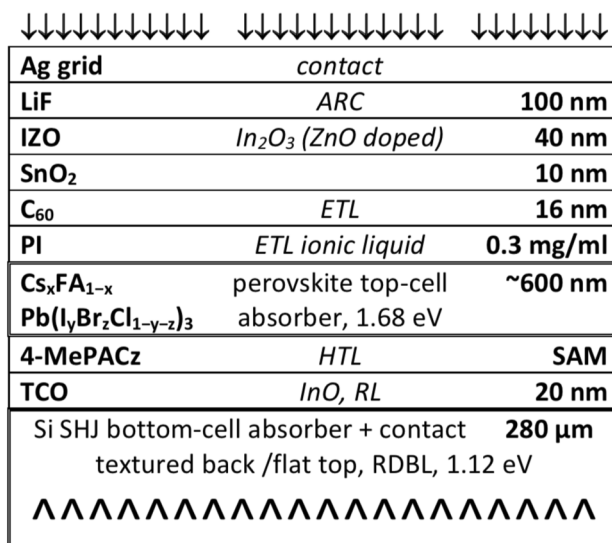


Fig. 14 Schematic representation of the stack structure of the 32.5% PCE device (See also Table 1). Layer thicknesses are indicated as well as function and band gap (as extracted from ref [75]). Note that the perovskite layer is sandwiched between 4-MePACz and PI (see Fig. 13 for their structures). ARC = anti-reflection coating; ETL = electron transport layer; HTL = hole transport layer; SAM = self-assembled monolayer; TCO = transparent conductive oxide; RL = recombination layer; RDBL = reflector with dielectric buffer layer. Top illumination and textured bottom. See reference [75] for more details

References

- Khan, F., Al-Ahmed, A., & Al-Sulaiman, F. A. (2021). Critical analysis of the limitations and validity of the assumptions with the analytical methods commonly used to determine the photovoltaic cell parameters. *Renewable and Sustainable Energy Reviews*, 140, 110753. <https://doi.org/10.1016/j.rser.2021.110753>
- Gielen, D., Boshell, F., Saygin, D., Bazilian, M. D., Wagner, N., & Gorini, R. (2019). The role of renewable energy in the global energy transformation. *Energy Strategy Reviews*, 24, 38–50. <https://doi.org/10.1016/j.esr.2019.01.006>
- Solar Energy Technologies Office. (2023, January 26). *Solar Photovoltaic Cell Basics* [US Gov website]. Office of Energy Efficiency & Renewable Energy. <https://www.energy.gov/eere/solar/solar-photovoltaic-cell-basics#:~:text=Silicon,of%20the%20modules%20sold%20today>.
- Shockley, W., & Queisser, H. J. (1961). Detailed Balance Limit of Efficiency of *p-n* Junction Solar Cells. *Journal of Applied Physics*, 32(3), 510–519. <https://doi.org/10.1063/1.1736034>
- Richter, A., Hermle, M., & Glunz, S. W. (2013). Reassessment of the Limiting Efficiency for Crystalline Silicon Solar Cells. *IEEE Journal of Photovoltaics*, 3(4), 1184–1191. <https://doi.org/10.1109/JPHOTOV.2013.2270351>
- National Renewable Energy Laboratory. (2023, October). *Best Research-Cell Efficiency Chart*. <https://www.nrel.gov/pv/cell-efficiency.html>
- Leijtens, T., Bush, K. A., Prasanna, R., & McGehee, M. D. (2018). Opportunities and challenges for tandem solar cells using metal halide perovskite semiconductors. *Nature Energy*, 3(10), 828–838. <https://doi.org/10.1038/s41560-018-0190-4>

8. Futscher, M. H., & Ehrler, B. (2016). Efficiency Limit of Perovskite/Si Tandem Solar Cells. *ACS Energy Letters*, 1(4), 863–868. <https://doi.org/10.1021/acseenergylett.6b00405>
9. Li, X., Xu, Q., Yan, L., Ren, C., Shi, B., Wang, P., Mazumdar, S., Hou, G., Zhao, Y., & Zhang, X. (2021). Silicon heterojunction-based tandem solar cells: Past, status, and future prospects. *Nanophotonics*, 10(8), 2001–2022. <https://doi.org/10.1515/nanoph-2021-0034>
10. Li, H., & Zhang, W. (2020). Perovskite Tandem Solar Cells: From Fundamentals to Commercial Deployment. *Chemical Reviews*, 120, 9835.
11. Brinkmann, K. O., Becker, T., Zimmermann, F., Kreuzel, C., Gahlmann, T., Theisen, M., Haeger, T., Olthof, S., Tückmantel, C., Günster, M., Maschwitz, T., Göbelsmann, F., Koch, C., Hertel, D., Caprioglio, P., Peña-Camargo, F., Perdígón-Toro, L., Al-Ashouri, A., Merten, L., & Riedl, T. (2022). Perovskite–organic tandem solar cells with indium oxide interconnect. *Nature*, 604(7905), 280–286. <https://doi.org/10.1038/s41586-022-04455-0>
12. Brakkee, R., & Williams, R. M. (2020). Minimizing Defect States in Lead Halide Perovskite Solar Cell Materials. *Applied Sciences*, 10(9), 3061. <https://doi.org/10.3390/app10093061>
13. Kojima, A., Teshima, K., Shirai, Y., & Miyasaka, T. (2009). Organometal Halide Perovskites as Visible-Light Sensitizers for Photovoltaic Cells. *Journal of the American Chemical Society*, 131(17), 6050–6051. <https://doi.org/10.1021/ja809598r>
14. Kim, J. Y., Lee, J.-W., Jung, H. S., Shin, H., & Park, N.-G. (2020). High-Efficiency Perovskite Solar Cells. *Chemical Reviews*, 120(15), 7867–7918. <https://doi.org/10.1021/acs.chemrev.0c00107>
15. Kim, H.-S., Lee, C.-R., Im, J.-H., Lee, K.-B., Moehl, T., Marchioro, A., Moon, S.-J., Humphry-Baker, R., Yum, J.-H., Moser, J. E., Grätzel, M., & Park, N.-G. (2012). Lead Iodide Perovskite Sensitized All-Solid-State Submicron Thin Film Mesoscopic Solar Cell with Efficiency Exceeding 9%. *Scientific Reports*, 2(1), 591. <https://doi.org/10.1038/srep00591>
16. Xiao, Z., Dong, Q., Bi, C., Shao, Y., Yuan, Y., & Huang, J. (2014). Solvent Annealing of Perovskite-Induced Crystal Growth for Photovoltaic-Device Efficiency Enhancement. *Advanced Materials*, 26(37), 6503–6509. <https://doi.org/10.1002/adma.201401685>
17. Bi, C., Wang, Q., Shao, Y., Yuan, Y., Xiao, Z., & Huang, J. (2015). Non-wetting surface-driven high-aspect-ratio crystalline grain growth for efficient hybrid perovskite solar cells. *Nature Communications*, 6(1), 7747. <https://doi.org/10.1038/ncomms8747>
18. Jeng, J.-Y., Chen, K.-C., Chiang, T.-Y., Lin, P.-Y., Tsai, T.-D., Chang, Y.-C., Guo, T.-F., Chen, P., Wen, T.-C., & Hsu, Y.-J. (2014). Nickel Oxide Electrode Interlayer in CH₃NH₃PbI₃ Perovskite/PCBM Planar-Heterojunction Hybrid Solar Cells. *Advanced Materials*, 26(24), 4107–4113. <https://doi.org/10.1002/adma.201306217>
19. Ossila. (2023, March 1). *Perovskites and Perovskite Solar Cells: An Introduction*. Ossila.Com. <https://www.ossila.com/en-eu/pages/perovskites-and-perovskite-solar-cells-an-introduction>
20. Guillemoles, J.-F., Kirchartz, T., Cahen, D., & Rau, U. (2019). Guide for the perplexed to the Shockley-Queisser model for solar cells. *Nature Photonics*, 13(8), 501–505. <https://doi.org/10.1038/s41566-019-0479-2>
21. Williams, R. M. (Director). (2020). *The Shockley-Queisser Limit: Theoretical limits of solar cells and how to surpass them*. <https://youtu.be/KsP90hT41t4>
22. Vos, A. D. (1980). Detailed balance limit of the efficiency of tandem solar cells. *Journal of Physics D: Applied Physics*, 13(5), 839–846. <https://doi.org/10.1088/0022-3727/13/5/018>
23. Ho-Baillie, A. W. Y., Zheng, J., Mahmud, M. A., Ma, F.-J., McKenzie, D. R., & Green, M. A. (2021). Recent progress and future prospects of perovskite tandem solar cells. *Applied Physics Reviews*, 8(4), 041307. <https://doi.org/10.1063/5.0061483>
24. Tockhorn, P., Wagner, P., Kegelmann, L., Stang, J.-C., Mews, M., Albrecht, S., & Korte, L. (2020). Three-Terminal Perovskite/Silicon Tandem Solar Cells with Top and Interdigitated Rear Contacts. *ACS Applied Energy Materials*, 3(2), 1381–1392. <https://doi.org/10.1021/acsaem.9b01800>
25. Rienäcker, M., Warren, E. L., Schnabel, M., Schulte-Huxel, H., Niepelt, R., Brendel, R., Stradins, P., Tamboli, A. C., & Peibst, R. (2019). Back-contacted bottom cells with three terminals: Maximizing power extraction from current-mismatched tandem cells. *Progress in Photovoltaics: Research and Applications*, 27(5), 410–423. <https://doi.org/10.1002/pip.3107>
26. Schuster, O., Wientjes, P., Shrestha, S., Levchuk, I., Sytnyk, M., Matt, G. J., Osvet, A., Batentschuk, M., Heiss, W., Brabec, C. J., Fauster, T., & Niesner, D. (2020). Looking beyond the Surface: The Band Gap of Bulk Methylammonium Lead Iodide. *Nano Letters*, 20(5), 3090–3097. <https://doi.org/10.1021/acs.nanolett.9b05068>
27. Zhu, H., Pan, L., Eickemeyer, F. T., Hope, M. A., Ouellette, O., Alanazi, A. Q. M., Gao, J., Baumeler, T. P., Li, X., Wang, S., Zakeeruddin, S. M., Liu, Y., Emsley, L., & Grätzel, M. (2022). Efficient and Stable Large Bandgap MAPbBr₃ Perovskite Solar Cell Attaining an Open Circuit Voltage of 1.65 V. *ACS Energy Letters*, 7(3), 1112–1119. <https://doi.org/10.1021/acsenergylett.1c02431>
28. Cheacharoen, R., Boyd, C. C., Burkhard, G. F., Leijtens, T., Raiford, J. A., Bush, K. A., Bent, S. F., & McGehee, M. D. (2018). Encapsulating perovskite solar cells to withstand damp heat and thermal cycling. *Sustainable Energy & Fuels*, 2(11), 2398–2406. <https://doi.org/10.1039/C8SE00250A>
29. Martins, J., Emami, S., Madureira, R., Mendes, J., Ivanou, D., & Mendes, A. (2020). Novel laser-assisted glass frit encapsulation for long-lifetime perovskite solar cells. *Journal of Materials Chemistry A*, 8(38), 20037–20046. <https://doi.org/10.1039/D0TA05583B>
30. Xu, T., Chen, Y., & Chen, Q. (2023). Improving intrinsic stability for perovskite/silicon tandem solar cells. *Science China Physics, Mechanics & Astronomy*, 66(1), 217305. <https://doi.org/10.1007/s11433-022-1959-4>
31. Hoke, E. T., Slotcavage, D. J., Dohner, E. R., Bowring, A. R., Karunadasa, H. L., & McGehee, M. D. (2015). Reversible photo-induced trap formation in mixed-halide hybrid perovskites for photovoltaics. *Chemical Science*, 6(1), 613–617. <https://doi.org/10.1039/C4SC03141E>
32. Fu, F., Li, J., Yang, T. C., Liang, H., Faes, A., Jeangros, Q., Ballif, C., & Hou, Y. (2022). Monolithic Perovskite-Silicon Tandem Solar Cells: From the Lab to Fab? *Advanced Materials*, 34(24), 2106540. <https://doi.org/10.1002/adma.202106540>
33. Shi, L., Bucknall, M. P., Young, T. L., Zhang, M., Hu, L., Bing, J., Lee, D. S., Kim, J., Wu, T., Takamure, N., McKenzie, D. R., Huang, S., Green, M. A., & Ho-Baillie, A. W. Y. (2020). Gas chromatography–mass spectrometry analyses of encapsulated stable perovskite solar cells. *Science*, 368(6497), eaba2412. <https://doi.org/10.1126/science.aba2412>
34. Essig, S., Allebé, C., Remo, T., Geisz, J. F., Steiner, M. A., Horowitz, K., Barraud, L., Ward, J. S., Schnabel, M., Descoedres, A., Young, D. L., Woodhouse, M., Despeisse, M., Ballif, C., & Tamboli, A. (2017). Raising the one-sun conversion efficiency of III–V/Si solar cells to 32.8% for two junctions and 35.9% for three junctions. *Nature Energy*, 2(9), 17144. <https://doi.org/10.1038/nenergy.2017.144>

35. Papež, N., Dallaev, R., Țălu, Ș., & Kaštyl, J. (2021). Overview of the Current State of Gallium Arsenide-Based Solar Cells. *Materials*, *14*(11), 3075. <https://doi.org/10.3390/ma14113075>
36. Mailoa, J. P., Bailie, C. D., Johlin, E. C., Hoke, E. T., Akey, A. J., Nguyen, W. H., McGehee, M. D., & Buonassisi, T. (2015). A 2-terminal perovskite/silicon multijunction solar cell enabled by a silicon tunnel junction. *Applied Physics Letters*, *106*(12), 121105. <https://doi.org/10.1063/1.4914179>
37. Bailie, C. D., Christoforo, M. G., Mailoa, J. P., Bowering, A. R., Unger, E. L., Nguyen, W. H., Burschka, J., Pellet, N., Lee, J. Z., Grätzel, M., Noufi, R., Buonassisi, T., Salleo, A., & McGehee, M. D. (2015). Semi-transparent perovskite solar cells for tandems with silicon and CIGS. *Energy & Environmental Science*, *8*(3), 956–963. <https://doi.org/10.1039/C4EE03322A>
38. Albrecht, S., Saliba, M., Correa Baena, J. P., Lang, F., Kegelmann, L., Mews, M., Steier, L., Abate, A., Rappich, J., Korte, L., Schlattmann, R., Nazeeruddin, M. K., Hagfeldt, A., Grätzel, M., & Rech, B. (2016). Monolithic perovskite/silicon-heterojunction tandem solar cells processed at low temperature. *Energy & Environmental Science*, *9*(1), 81–88. <https://doi.org/10.1039/C5EE02965A>
39. Hawash, Z., Ono, L. K., Raga, S. R., Lee, M. V., & Qi, Y. (2015). Air-Exposure Induced Dopant Redistribution and Energy Level Shifts in Spin-Coated Spiro-MeOTAD Films. *Chemistry of Materials*, *27*(2), 562–569. <https://doi.org/10.1021/cm504022q>
40. Abate, A., Leijtens, T., Pathak, S., Teuscher, J., Avolio, R., Errico, M. E., Kirkpatrick, J., Ball, J. M., Docampo, P., McPherson, I., & Snaith, H. J. (2013). Lithium salts as “redox active” p-type dopants for organic semiconductors and their impact in solid-state dye-sensitized solar cells. *Physical Chemistry Chemical Physics*, *15*(7), 2572. <https://doi.org/10.1039/c2cp44397j>
41. Xu, J., Voznyy, O., Comin, R., Gong, X., Walters, G., Liu, M., Kanjanaboons, P., Lan, X., & Sargent, E. H. (2016). Crosslinked Remote-Doped Hole-Extracting Contacts Enhance Stability under Accelerated Lifetime Testing in Perovskite Solar Cells. *Advanced Materials*, *28*(14), 2807–2815. <https://doi.org/10.1002/adma.201505630>
42. Bush, K. A., Palmstrom, A. F., Yu, Z. J., Boccard, M., Cheacharoen, R., Mailoa, J. P., McMeekin, D. P., Hoye, R. L. Z., Bailie, C. D., Leijtens, T., Peters, I. M., Minichetti, M. C., Rolston, N., Prasanna, R., Sofia, S., Harwood, D., Ma, W., Moghadam, F., Snaith, H. J., & McGehee, M. D. (2017). 23.6%-efficient monolithic perovskite/silicon tandem solar cells with improved stability. *Nature Energy*, *2*(4), 17009. <https://doi.org/10.1038/nenergy.2017.9>
43. You, J., Meng, L., Song, T.-B., Guo, T.-F., Yang, Y., Chang, W.-H., Hong, Z., Chen, H., Zhou, H., Chen, Q., Liu, Y., De Marco, N., & Yang, Y. (2016). Improved air stability of perovskite solar cells via solution-processed metal oxide transport layers. *Nature Nanotechnology*, *11*(1), 75–81. <https://doi.org/10.1038/nnano.2015.230>
44. Slotcavage, D. J., Karunadasa, H. I., & McGehee, M. D. (2016). Light-Induced Phase Segregation in Halide-Perovskite Absorbers. *ACS Energy Letters*, *1*(6), 1199–1205. <https://doi.org/10.1021/acsenenergylett.6b00495>
45. Yao, Y., Hang, P., Li, B., Hu, Z., Kan, C., Xie, J., Wang, Y., Zhang, Y., Yang, D., & Yu, X. (2022). Phase-Stable Wide-Bandgap Perovskites for Four-Terminal Perovskite/Silicon Tandem Solar Cells with Over 30% Efficiency. *Small (Weinheim an der Bergstrasse, Germany)*, *18*(38), 2203319. <https://doi.org/10.1002/sml.202203319>
46. Unger, E. L., Kegelmann, L., Suchan, K., Sörell, D., Korte, L., & Albrecht, S. (2017). Roadmap and roadblocks for the band gap tunability of metal halide perovskites. *Journal of Materials Chemistry A*, *5*(23), 11401–11409. <https://doi.org/10.1039/C7TA00404D>
47. Anaya, M., Lozano, G., Calvo, M. E., & Míguez, H. (2017). ABX3 Perovskites for Tandem Solar Cells. *Joule*, *1*(4), 769–793. <https://doi.org/10.1016/j.joule.2017.09.017>
48. De Bastiani, M., Dell’Erba, G., Gandini, M., D’Innocenzo, V., Neutzner, S., Kandada, A. R. S., Grancini, G., Binda, M., Prato, M., Ball, J. M., Caironi, M., & Petrozza, A. (2016). Ion Migration and the Role of Preconditioning Cycles in the Stabilization of the J – V Characteristics of Inverted Hybrid Perovskite Solar Cells. *Advanced Energy Materials*, *6*(2), 1501453. <https://doi.org/10.1002/aenm.201501453>
49. Chen, S., Xiao, X., Gu, H., & Huang, J. (2021). Iodine reduction for reproducible and high-performance perovskite solar cells and modules. *Science Advances*, *7*(10), eabe8130. <https://doi.org/10.1126/sciadv.abe8130>
50. Liu, J., De Bastiani, M., Aydin, E., Harrison, G. T., Gao, Y., Pradhan, R. R., Eswaran, M. K., Mandal, M., Yan, W., Seitkhan, A., Babics, M., Subbiah, A. S., Ugur, E., Xu, F., Xu, L., Wang, M., Rehman, A. U. R., Razaq, A., Kang, J., & De Wolf, S. (2022). Efficient and stable perovskite-silicon tandem solar cells through contact displacement by MgFx. *Science*, *377*(6603), 302–306. <https://doi.org/10.1126/science.abn8910>
51. Yang, G., Ni, Z., Yu, Z. J., Larson, B. W., Yu, Z., Chen, B., Alasfour, A., Xiao, X., Luther, J. M., Holman, Z. C., & Huang, J. (2022). Defect engineering in wide-bandgap perovskites for efficient perovskite-silicon tandem solar cells. *Nature Photonics*, *16*(8), 588–594. <https://doi.org/10.1038/s41566-022-01033-8>
52. Mahesh, S., Ball, J. M., Oliver, R. D. J., McMeekin, D. P., Nayak, P. K., Johnston, M. B., & Snaith, H. J. (2020). Revealing the origin of voltage loss in mixed-halide perovskite solar cells. *Energy & Environmental Science*, *13*(1), 258–267. <https://doi.org/10.1039/C9EE02162K>
53. Ni, Z., Jiao, H., Fei, C., Gu, H., Xu, S., Yu, Z., Yang, G., Deng, Y., Jiang, Q., Liu, Y., Yan, Y., & Huang, J. (2021). Evolution of defects during the degradation of metal halide perovskite solar cells under reverse bias and illumination. *Nature Energy*, *7*(1), 65–73. <https://doi.org/10.1038/s41560-021-00949-9>
54. Meggiolaro, D., Motti, S. G., Mosconi, E., Barker, A. J., Ball, J., Perini, A. R., & C., Deschler, F., Petrozza, A., & De Angelis, F. (2018). Iodine chemistry determines the defect tolerance of lead-halide perovskites. *Energy & Environmental Science*, *11*(3), 702–713. <https://doi.org/10.1039/C8EE00124C>
55. Zhao, Y., Miao, P., Elia, J., Hu, H., Wang, X., Heumueller, T., Hou, Y., Matt, G. J., Osvet, A., Chen, Y.-T., Tarragó, M., de Ligny, D., Przybilla, T., Denninger, P., Will, J., Zhang, J., Tang, X., Li, N., He, C., & Brabec, C. J. (2020). Strain-activated light-induced halide segregation in mixed-halide perovskite solids. *Nature Communications*, *11*(1), 6328. <https://doi.org/10.1038/s41467-020-20066-7>
56. Zhang, Z., Li, Z., Meng, L., Lien, S., & Gao, P. (2020). Perovskite-Based Tandem Solar Cells: Get the Most Out of the Sun. *Advanced Functional Materials*, *30*(38), 2001904. <https://doi.org/10.1002/adfm.202001904>
57. Turren-Cruz, S.-H., Hagfeldt, A., & Saliba, M. (2018). Methylammonium-free, high-performance, and stable perovskite solar cells on a planar architecture. *Science*, *362*(6413), 449–453. <https://doi.org/10.1126/science.aat3583>
58. Rehman, W., McMeekin, D. P., Patel, J. B., Milot, R. L., Johnston, M. B., Snaith, H. J., & Herz, L. M. (2017). Photovoltaic mixed-cation lead mixed-halide perovskites: Links between crystallinity, photo-stability and electronic properties. *Energy & Environmental Science*, *10*(1), 361–369. <https://doi.org/10.1039/C6EE03014A>
59. Saliba, M., Matsui, T., Seo, J.-Y., Domanski, K., Correa-Baena, J.-P., Nazeeruddin, M. K., Zakeeruddin, S. M., Tress, W., Abate, A., Hagfeldt, A., & Grätzel, M. (2016). Cesium-containing triple cation perovskite solar cells: Improved stability, reproducibility

- and high efficiency. *Energy & Environmental Science*, 9(6), 1989–1997. <https://doi.org/10.1039/C5EE03874J>
60. Duong, T., Mulmudi, H. K., Wu, Y., Fu, X., Shen, H., Peng, J., Wu, N., Nguyen, H. T., Macdonald, D., Lockrey, M., White, T. P., Weber, K., & Catchpole, K. (2017). Light and Electrically Induced Phase Segregation and Its Impact on the Stability of Quadruple Cation High Bandgap Perovskite Solar Cells. *ACS Applied Materials & Interfaces*, 9(32), 26859–26866. <https://doi.org/10.1021/acsami.7b06816>
 61. Bella, F., Renzi, P., Cavallo, C., & Gerbaldi, C. (2018). Caesium for Perovskite Solar Cells: An Overview. *Chemistry - A European Journal*, 24(47), 12183–12205. <https://doi.org/10.1002/chem.201801096>
 62. Bush, K. A., Rolston, N., Gold-Parker, A., Manzoor, S., Hausele, J., Yu, Z. J., Raiford, J. A., Cheacharoen, R., Holman, Z. C., Toney, M. F., Dauskardt, R. H., & McGehee, M. D. (2018). Controlling Thin-Film Stress and Wrinkling during Perovskite Film Formation. *ACS Energy Letters*, 3(6), 1225–1232. <https://doi.org/10.1021/acsenenergylett.8b00544>
 63. Li, Z., Yang, M., Park, J.-S., Wei, S.-H., Berry, J. J., & Zhu, K. (2016). Stabilizing Perovskite Structures by Tuning Tolerance Factor: Formation of Formamidinium and Cesium Lead Iodide Solid-State Alloys. *Chemistry of Materials*, 28(1), 284–292. <https://doi.org/10.1021/acs.chemmater.5b04107>
 64. Duong, T., Mulmudi, H. K., Shen, H., Wu, Y., Barugkin, C., Mayon, Y. O., Nguyen, H. T., Macdonald, D., Peng, J., Lockrey, M., Li, W., Cheng, Y.-B., White, T. P., Weber, K., & Catchpole, K. (2016). Structural engineering using rubidium iodide as a dopant under excess lead iodide conditions for high efficiency and stable perovskites. *Nano Energy*, 30, 330–340. <https://doi.org/10.1016/j.nanoen.2016.10.027>
 65. Zhang, M., Yun, J. S., Ma, Q., Zheng, J., Lau, C. F. J., Deng, X., Kim, J., Kim, D., Seidel, J., Green, M. A., Huang, S., & Ho-Baillie, A. W. Y. (2017). High-Efficiency Rubidium-Incorporated Perovskite Solar Cells by Gas Quenching. *ACS Energy Letters*, 2(2), 438–444. <https://doi.org/10.1021/acsenenergylett.6b00697>
 66. Hu, Y., Aygüler, M. F., Petrus, M. L., Bein, T., & Docampo, P. (2017). Impact of Rubidium and Cesium Cations on the Moisture Stability of Multiple-Cation Mixed-Halide Perovskites. *ACS Energy Letters*, 2(10), 2212–2218. <https://doi.org/10.1021/acsenenergylett.7b00731>
 67. Liang, P.-W., Chueh, C.-C., Xin, X.-K., Zuo, F., Williams, S. T., Liao, C.-Y., & Jen, A.K.-Y. (2015). High-Performance Planar-Heterojunction Solar Cells Based on Ternary Halide Large-Band-Gap Perovskites. *Advanced Energy Materials*, 5(1), 1400960. <https://doi.org/10.1002/aenm.201400960>
 68. Colella, S., Mosconi, E., Fedeli, P., Listorti, A., Gazza, F., Orlandi, F., Ferro, P., Besagni, T., Rizzo, A., Calestani, G., Gigli, G., De Angelis, F., & Mosca, R. (2013). MAPbI_{3-x}Cl_x Mixed Halide Perovskite for Hybrid Solar Cells: The Role of Chloride as Dopant on the Transport and Structural Properties. *Chemistry of Materials*, 25(22), 4613–4618. <https://doi.org/10.1021/cm402919x>
 69. Dastidar, S., Egger, D. A., Tan, L. Z., Cromer, S. B., Dillon, A. D., Liu, S., Kronik, L., Rappe, A. M., & Fafarman, A. T. (2016). High Chloride Doping Levels Stabilize the Perovskite Phase of Cesium Lead Iodide. *Nano Letters*, 16(6), 3563–3570. <https://doi.org/10.1021/acs.nanolett.6b00635>
 70. Saidaminov, M. I., Kim, J., Jain, A., Quintero-Bermudez, R., Tan, H., Long, G., Tan, F., Johnston, A., Zhao, Y., Voznyy, O., & Sargent, E. H. (2018). Suppression of atomic vacancies via incorporation of isovalent small ions to increase the stability of halide perovskite solar cells in ambient air. *Nature Energy*, 3(8), 648–654. <https://doi.org/10.1038/s41560-018-0192-2>
 71. Xu, J., Boyd, C. C., Yu, Z. J., Palmstrom, A. F., Witter, D. J., Larson, B. W., France, R. M., Werner, J., Harvey, S. P., Wolf, E. J., Weigand, W., Manzoor, S., van Hest, M. F. A. M., Berry, J. J., Luther, J. M., Holman, Z. C., & McGehee, M. D. (2020). Triple-halide wide-band gap perovskites with suppressed phase segregation for efficient tandems. *Science*, 367(6482), 1097–1104. <https://doi.org/10.1126/science.aaz5074>
 72. Wen, J., Zhao, Y., Liu, Z., Gao, H., Lin, R., Wan, S., Ji, C., Xiao, K., Gao, Y., Tian, Y., Xie, J., Brabec, C. J., & Tan, H. (2022). Steric Engineering Enables Efficient and Photostable Wide-Bandgap Perovskites for All-Perovskite Tandem Solar Cells. *Advanced Materials*, 34(26), 2110356. <https://doi.org/10.1002/adma.202110356>
 73. Zhu, Z., Mao, K., & Xu, J. (2021). Perovskite tandem solar cells with improved efficiency and stability. *Journal of Energy Chemistry*, 58, 219–232. <https://doi.org/10.1016/j.jechem.2020.09.022>
 74. Afshari, H., Sourabh, S., Chacon, S. A., Whiteside, V. R., Penner, R. C., Rout, B., Kirmani, A. R., Luther, J. M., Eperon, G. E., & Sellers, I. R. (2023). FACsPb Triple Halide Perovskite Solar Cells with Thermal Operation over 200 °C. *ACS Energy Letters*, 8(5), 2408–2413. <https://doi.org/10.1021/acsenenergylett.3c00551>
 75. Mariotti, S., Köhnen, E., Scheler, F., Sveinbjörnsson, K., Zimmermann, L., Piot, M., Yang, F., Li, B., Warby, J., Musienko, A., Menzel, D., Lang, F., Keßler, S., Levine, I., Mantione, D., Al-Ashouri, A., Härtel, M. S., Xu, K., Cruz, A., & Albrecht, S. (2023). Interface engineering for high-performance, triple-halide perovskite–silicon tandem solar cells. *Science*, 381(6653), 63–69. <https://doi.org/10.1126/science.adf5872>
 76. Wang, R., Xue, J., Wang, K.-L., Wang, Z.-K., Luo, Y., Fenning, D., Xu, G., Nuryyeva, S., Huang, T., Zhao, Y., Yang, J. L., Zhu, J., Wang, M., Tan, S., Yavuz, I., Houk, K. N., & Yang, Y. (2019). Constructive molecular configurations for surface-defect passivation of perovskite photovoltaics. *Science*, 366(6472), 1509–1513. <https://doi.org/10.1126/science.aay9698>
 77. Bai, S., Da, P., Li, C., Wang, Z., Yuan, Z., Fu, F., Kawecki, M., Liu, X., Sakai, N., Wang, J.T.-W., Huettner, S., Buecheler, S., Fahlman, M., Gao, F., & Snaith, H. J. (2019). Planar perovskite solar cells with long-term stability using ionic liquid additives. *Nature*, 571(7764), 245–250. <https://doi.org/10.1038/s41586-019-1357-2>
 78. Lin, Y.-H., Sakai, N., Da, P., Wu, J., Sansom, H. C., Ramadan, A. J., Mahesh, S., Liu, J., Oliver, R. D. J., Lim, J., Aspirtarte, L., Sharma, K., Madhu, P. K., Morales-Vilches, A. B., Nayak, P. K., Bai, S., Gao, F., Grovenor, C. R. M., Johnston, M. B., & Snaith, H. J. (2020). A piperidinium salt stabilizes efficient metal-halide perovskite solar cells. *Science*, 369(6499), 96–102. <https://doi.org/10.1126/science.abal628>
 79. Liu, J., Aydin, E., Yin, J., De Bastiani, M., Isikgor, F. H., Rehman, A. U., Yengel, E., Ugur, E., Harrison, G. T., Wang, M., Gao, Y., Khan, J. I., Babics, M., Allen, T. G., Subbiah, A. S., Zhu, K., Zheng, X., Yan, W., Xu, F., & De Wolf, S. (2021). 28.2%-efficient, outdoor-stable perovskite/silicon tandem solar cell. *Joule*, 5(12), 3169–3186. <https://doi.org/10.1016/j.joule.2021.11.003>
 80. Al-Ashouri, A., Köhnen, E., Li, B., Magomedov, A., Hempel, H., Caprioglio, P., Márquez, J. A., Morales Vilches, A. B., Kasparavicius, E., Smith, J. A., Phung, N., Menzel, D., Grischek, M., Kegelmann, L., Skroblin, D., Gollwitzer, C., Malinauskas, T., Jošt, M., Matič, G., & Albrecht, S. (2020). Monolithic perovskite/silicon tandem solar cell with >29% efficiency by enhanced hole extraction. *Science*, 370(6522), 1300–1309. <https://doi.org/10.1126/science.abd4016>
 81. Köhnen, E., Wagner, P., Lang, F., Cruz, A., Li, B., Roß, M., Jošt, M., Morales-Vilches, A. B., Topič, M., Stolterfoht, M., Neher, D., Korte, L., Rech, B., Schlattmann, R., Stannowski, B., & Albrecht, S. (2021). 27.9% Efficient Monolithic Perovskite/Silicon Tandem Solar Cells on Industry Compatible Bottom Cells. *Solar RRL*, 5(7), 2100244. <https://doi.org/10.1002/solr.202100244>

82. Lin, Y., Bai, Y., Fang, Y., Chen, Z., Yang, S., Zheng, X., Tang, S., Liu, Y., Zhao, J., & Huang, J. (2018). Enhanced Thermal Stability in Perovskite Solar Cells by Assembling 2D/3D Stacking Structures. *The Journal of Physical Chemistry Letters*, 9(3), 654–658. <https://doi.org/10.1021/acs.jpcclett.7b02679>
83. Yang, G., Ren, Z., Liu, K., Qin, M., Deng, W., Zhang, H., Wang, H., Liang, J., Ye, F., Liang, Q., Yin, H., Chen, Y., Zhuang, Y., Li, S., Gao, B., Wang, J., Shi, T., Wang, X., Lu, X., & Li, G. (2021). Stable and low-photovoltage-loss perovskite solar cells by multifunctional passivation. *Nature Photonics*, 15(9), 681–689. <https://doi.org/10.1038/s41566-021-00829-4>
84. Duong, T., Pham, H., Kho, T. C., Phang, P., Fong, K. C., Yan, D., Yin, Y., Peng, J., Mahmud, M. A., Gharibzadeh, S., Nejad, B. A., Hossain, I. M., Khan, M. R., Mozaffari, N., Wu, Y., Shen, H., Zheng, J., Mai, H., Liang, W., & Catchpole, K. (2020). High Efficiency Perovskite-Silicon Tandem Solar Cells: Effect of Surface Coating versus Bulk Incorporation of 2D Perovskite. *Advanced Energy Materials*, 10(9), 1903553. <https://doi.org/10.1002/aenm.201903553>
85. Sutanto, A. A., Caprioglio, P., Drigo, N., Hofstetter, Y. J., Garcia-Benito, I., Queloz, V. I. E., Neher, D., Nazeeruddin, M. K., Stolterfoht, M., Vaynzof, Y., & Grancini, G. (2021). 2D/3D perovskite engineering eliminates interfacial recombination losses in hybrid perovskite solar cells. *Chem*, 7(7), 1903–1916. <https://doi.org/10.1016/j.chempr.2021.04.002>
86. Xu, Q., Shi, B., Li, Y., Yan, L., Duan, W., Li, Y., Li, R., Ren, N., Han, W., Liu, J., Huang, Q., Zhang, D., Ren, H., Xu, S., Zhang, C., Zhuang, H., Lambertz, A., Ding, K., Zhao, Y., & Zhang, X. (2022). Conductive Passivator for Efficient Monolithic Perovskite/Silicon Tandem Solar Cell on Commercially Textured Silicon. *Advanced Energy Materials*, 12(46), 2202404. <https://doi.org/10.1002/aenm.202202404>
87. Kim, D., Jung, H. J., Park, I. J., Larson, B. W., Dunfield, S. P., Xiao, C., Kim, J., Tong, J., Boonmongkolras, P., Ji, S. G., Zhang, F., Pae, S. R., Kim, M., Kang, S. B., Dravid, V., Berry, J. J., Kim, J. Y., Zhu, K., Kim, D. H., & Shin, B. (2020). Efficient, stable silicon tandem cells enabled by anion-engineered wide-bandgap perovskites. *Science*, 368(6487), 155–160. <https://doi.org/10.1126/science.aba3433>
88. Yan, L., Qiu, S., Yu, B., Huang, J., Qiu, J., Zhang, C., Guo, F., Yang, Y., & Mai, Y. (2022). Synergistic Passivation of Perovskite Absorber Films for Efficient Four-Terminal Perovskite/Silicon Tandem Solar Cells. *Advanced Energy and Sustainability Research*, 3(6), 2100199. <https://doi.org/10.1002/aesr.202100199>
89. Duong, T., Nguyen, T., Huang, K., Pham, H., Adhikari, S. G., Khan, M. R., Duan, L., Liang, W., Fong, K. C., Shen, H., Bui, A. D., Mayon, A. O., Truong, T., Tabi, G., Ahmad, V., Surve, S., Tong, J., Kho, T., Tran-Phu, T., & Catchpole, K. (2023). Bulk Incorporation with 4-Methylphenethylammonium Chloride for Efficient and Stable Methylammonium-Free Perovskite and Perovskite-Silicon Tandem Solar Cells. *Advanced Energy Materials*, 13(9), 2203607. <https://doi.org/10.1002/aenm.202203607>
90. Lee, D. S., Yun, J. S., Kim, J., Soufiani, A. M., Chen, S., Cho, Y., Deng, X., Seidel, J., Lim, S., Huang, S., & Ho-Baillie, A. W. Y. (2018). Passivation of Grain Boundaries by Phenethylammonium in Formamidinium-Methylammonium Lead Halide Perovskite Solar Cells. *ACS Energy Letters*, 3(3), 647–654. <https://doi.org/10.1021/acsenenergylett.8b00121>
91. National Renewable Energy Laboratory. (2023). *Best Research-Cell Efficiency Chart*. National Renewable Energy Laboratory. <https://www.nrel.gov/pv/cell-efficiency.html/>
92. Aydin, E., Ugur, E., Yildirim, B. K., Allen, T. G., Dally, P., Razaq, A., Cao, F., Xu, L., Vishal, B., Yazmaciyan, A., Said, A. A., Zhumagali, S., Azmi, R., Babics, M., Fell, A., Xiao, C., & De Wolf, S. (2023). Enhanced optoelectronic coupling for perovskite-silicon tandem solar cells. *Nature*. <https://doi.org/10.1038/s41586-023-06667-4>
93. Chin, X. Y., Turkey, D., Steele, J. A., Tabean, S., Eswara, S., Mensi, M., Fiala, P., Wolff, C. M., Paracchino, A., Artuk, K., Jacobs, D., Guesnay, Q., Sahli, F., Andreatta, G., Boccard, M., Jeangros, Q., & Ballif, C. (2023). Interface passivation for 31.25%-efficient perovskite/silicon tandem solar cells. *Science*, 381(6653), 59–63. <https://doi.org/10.1126/science.adg0091>
94. Tockhorn, P., Sutter, J., Cruz, A., Wagner, P., Jäger, K., Yoo, D., Lang, F., Grischek, M., Li, B., Li, J., Shargaieva, O., Unger, E., Al-Ashouri, A., Köhnen, E., Stolterfoht, M., Neher, D., Schlattmann, R., Rech, B., Stannowski, B., & Becker, C. (2022). Nano-optical designs for high-efficiency monolithic perovskite-silicon tandem solar cells. *Nature Nanotechnology*, 17(11), 1214–1221. <https://doi.org/10.1038/s41565-022-01228-8>
95. Sveinbjörnsson, K., Li, B., Mariotti, S., Jarzembowski, E., Kegelmann, L., Wirtz, A., Frühauf, F., Weihrauch, A., Niemann, R., Korte, L., Fertig, F., Müller, J. W., & Albrecht, S. (2022). Monolithic Perovskite/Silicon Tandem Solar Cell with 28.7% Efficiency Using Industrial Silicon Bottom Cells. *ACS Energy Letters*, 7(8), 2654–2656. <https://doi.org/10.1021/acsenenergylett.2c01358>
96. Luo, X., Luo, H., Li, H., Xia, R., Zheng, X., Huang, Z., Liu, Z., Gao, H., Zhang, X., Li, S., Feng, Z., Chen, Y., & Tan, H. (2023). Efficient Perovskite/Silicon Tandem Solar Cells on Industrially Compatible Textured Silicon. *Advanced Materials*, 35(9), 2207883. <https://doi.org/10.1002/adma.202207883>
97. Zheng, J., Duan, W., Guo, Y., Zhao, Z. C., Yi, H., Ma, F.-J., Granados Caro, L., Yi, C., Bing, J., Tang, S., Qu, J., Fong, K. C., Cui, X., Zhu, Y., Yang, L., Lambertz, A., Ararat Mahmud, M., Chen, H., Liao, C., & Ho-Baillie, A. W. Y. (2023). Efficient monolithic perovskite-Si tandem solar cells enabled by an ultrathin indium tin oxide interlayer. *Energy & Environmental Science*. <https://doi.org/10.1039/D2EE04007G>
98. Hou, Y., Aydin, E., De Bastiani, M., Xiao, C., Isikgor, F. H., Xue, D.-J., Chen, B., Chen, H., Bahrami, B., Chowdhury, A. H., Johnston, A., Baek, S.-W., Huang, Z., Wei, M., Dong, Y., Troughton, J., Jalmood, R., Mirabelli, A. J., Allen, T. G., & Sargent, E. H. (2020). Efficient tandem solar cells with solution-processed perovskite on textured crystalline silicon. *Science*, 367(6482), 1135–1140. <https://doi.org/10.1126/science.aaz3691>
99. Nogay, G., Sahli, F., Werner, J., Monnard, R., Boccard, M., Despeisse, M., Haug, F.-J., Jeangros, Q., Ingenito, A., & Ballif, C. (2019). 25.1%-Efficient Monolithic Perovskite/Silicon Tandem Solar Cell Based on a p-type Monocrystalline Textured Silicon Wafer and High-Temperature Passivating Contacts. *ACS Energy Letters*, 4(4), 844–845. <https://doi.org/10.1021/acsenenergylett.9b00377>
100. Ji, S. G., Park, I. J., Chang, H., Park, J. H., Hong, G. P., Choi, B. K., Jang, J. H., Choi, Y. J., Lim, H. W., Ahn, Y. J., Park, S. J., Nam, K. T., Hyeon, T., Park, J., Kim, D. H., & Kim, J. Y. (2022). Stable pure-iodide wide-band-gap perovskites for efficient Si tandem cells via kinetically controlled phase evolution. *Joule*, 6(10), 2390–2405. <https://doi.org/10.1016/j.joule.2022.08.006>
101. Li, T., Xu, J., Lin, R., Teale, S., Li, H., Liu, Z., Duan, C., Zhao, Q., Xiao, K., Wu, P., Chen, B., Jiang, S., Xiong, S., Luo, H., Wan, S., Li, L., Bao, Q., Tian, Y., Gao, X., & Tan, H. (2023). Inorganic wide-bandgap perovskite subcells with dipole bridge for all-perovskite tandems. *Nature Energy*, 8(6), 610–620. <https://doi.org/10.1038/s41560-023-01250-7>
102. De Wolf, S., Descoeurdes, A., Holman, Z. C., & Ballif, C. (2012). High-efficiency Silicon Heterojunction Solar Cells: A Review. *Green*, 2(1), 7–24. <https://doi.org/10.1515/green-2011-0018>
103. Green, M. A. (2015). The Passivated Emitter and Rear Cell (PERC): From conception to mass production. *Solar Energy*

- Materials and Solar Cells*, 143, 190–197. <https://doi.org/10.1016/j.solmat.2015.06.055>
104. Dullweber, T., & Schmidt, J. (2016). Industrial Silicon Solar Cells Applying the Passivated Emitter and Rear Cell (PERC) Concept—A Review. *IEEE Journal of Photovoltaics*, 6(5), 1366–1381. <https://doi.org/10.1109/JPHOTOV.2016.2571627>
 105. Blakers, A. (2019). Development of the PERC Solar Cell. *IEEE Journal of Photovoltaics*, 9(3), 629–635. <https://doi.org/10.1109/JPHOTOV.2019.2899460>
 106. Baliozian, P., Tepner, S., Fischer, M., Trube, J., Herritsch, S., Gensowski, K., Clement, F., Nold, S., & Preu, R. (2020). The International Technology Roadmap for Photovoltaics and the Significance of Its Decade-Long Projections [Application/pdf]. *37th European Photovoltaic Solar Energy Conference and Exhibition; 420–426*, 7 pages, 11197 kb. <https://doi.org/10.4229/EUPVSEC20202020-2CV.1.59>
 107. Burschka, J., Pellet, N., Moon, S.-J., Humphry-Baker, R., Gao, P., Nazeeruddin, M. K., & Grätzel, M. (2013). Sequential deposition as a route to high-performance perovskite-sensitized solar cells. *Nature*, 499(7458), 316–319. <https://doi.org/10.1038/nature12340>
 108. Wu, Y., Yan, D., Peng, J., Duong, T., Wan, Y., Phang, S. P., Shen, H., Wu, N., Barugkin, C., Fu, X., Surve, S., Grant, D., Walter, D., White, T. P., Catchpole, K. R., & Weber, K. J. (2017). Monolithic perovskite/silicon-homojunction tandem solar cell with over 22% efficiency. *Energy & Environmental Science*, 10(11), 2472–2479. <https://doi.org/10.1039/C7EE02288C>
 109. Hoyer, R. L. Z., Bush, K. A., Oviedo, F., Sofia, S. E., Thway, M., Li, X., Liu, Z., Jean, J., Mailoa, J. P., Osherov, A., Lin, F., Palmstrom, A. F., Bulovic, V., McGehee, M. D., Peters, I. M., & Buonassisi, T. (2018). Developing a Robust Recombination Contact to Realize Monolithic Perovskite Tandems With Industrially Common p-Type Silicon Solar Cells. *IEEE Journal of Photovoltaics*, 8(4), 1023–1028. <https://doi.org/10.1109/JPHOTOV.2018.2820509>
 110. Werner, J., Walter, A., Rucavado, E., Moon, S.-J., Sacchetto, D., Rienaecker, M., Peibst, R., Brendel, R., Niquille, X., De Wolf, S., Löper, P., Morales-Masis, M., Nicolay, S., Niesen, B., & Ballif, C. (2016). Zinc tin oxide as high-temperature stable recombination layer for mesoscopic perovskite/silicon monolithic tandem solar cells. *Applied Physics Letters*, 109(23), 233902. <https://doi.org/10.1063/1.4971361>
 111. Taguchi, M., Yano, A., Tohoda, S., Matsuyama, K., Nakamura, Y., Nishiwaki, T., Fujita, K., & Maruyama, E. (2014). 24.7% Record Efficiency HIT Solar Cell on Thin Silicon Wafer. *IEEE Journal of Photovoltaics*, 4(1), 96–99. <https://doi.org/10.1109/JPHOTOV.2013.2282737>
 112. Holman, Z. C., Descoedres, A., De Wolf, S., & Ballif, C. (2013). Record Infrared Internal Quantum Efficiency in Silicon Heterojunction Solar Cells With Dielectric/Metal Rear Reflectors. *IEEE Journal of Photovoltaics*, 3(4), 1243–1249. <https://doi.org/10.1109/JPHOTOV.2013.2276484>
 113. Haschke, J., Dupré, O., Boccard, M., & Ballif, C. (2018). Silicon heterojunction solar cells: Recent technological development and practical aspects - from lab to industry. *Solar Energy Materials and Solar Cells*, 187, 140–153. <https://doi.org/10.1016/j.solmat.2018.07.018>
 114. Haschke, J., Seif, J. P., Riesen, Y., Tomasi, A., Cattin, J., Tous, L., Choulat, P., Aleman, M., Cornagliotti, E., Uruena, A., Russell, R., Duerinckx, F., Champiaud, J., Levrat, J., Abdallah, A. A., Aïssa, B., Tabet, N., Wyrsh, N., Despeisse, M., & Ballif, C. (2017). The impact of silicon solar cell architecture and cell interconnection on energy yield in hot & sunny climates. *Energy & Environmental Science*, 10(5), 1196–1206. <https://doi.org/10.1039/C7EE00286F>
 115. Walter, A., Kamino, B., Moon, S.-J., Wyss, P., Díaz León, J. J., Allebé, C., Descoedres, A., Nicolay, S., Ballif, C., Jeangros, Q., & Ingenito, A. (2023). Rear Textured p-type High Temperature Passivating Contacts and their Implementation in Perovskite/Silicon Tandem Cells. *Energy Advances*. <https://doi.org/10.1039/D3YA00048F>
 116. Wafer World. (2017, March 8). *Float Zone Silicon vs Czochralski Silicon | Which Is Better?* Wafer World. <https://www.waferworld.com/post/float-zone-silicon-vs-czochralski>
 117. Sahli, F., Werner, J., Kamino, B. A., Bräuninger, M., Monnard, R., Paviet-Salomon, B., Barraud, L., Ding, L., Diaz Leon, J. J., Sacchetto, D., Cattaneo, G., Despeisse, M., Boccard, M., Nicolay, S., Jeangros, Q., Niesen, B., & Ballif, C. (2018). Fully textured monolithic perovskite/silicon tandem solar cells with 25.2% power conversion efficiency. *Nature Materials*, 17(9), 820–826. <https://doi.org/10.1038/s41563-018-0115-4>
 118. Chen, B., Yu, Z. J., Manzoor, S., Wang, S., Weigand, W., Yu, Z., Yang, G., Ni, Z., Dai, X., Holman, Z. C., & Huang, J. (2020). Blade-Coated Perovskites on Textured Silicon for 26%-Efficient Monolithic Perovskite/Silicon Tandem Solar Cells. *Joule*, 4(4), 850–864. <https://doi.org/10.1016/j.joule.2020.01.008>
 119. De Bastiani, M., Jalmood, R., Liu, J., Ossig, C., Vlk, A., Vegso, K., Babics, M., Isikgor, F. H., Selvin, A. S., Azmi, R., Ugur, E., Banerjee, S., Mirabelli, A. J., Aydin, E., Allen, T. G., Ur Rehman, A., Van Kerschaver, E., Siffalovic, P., Stuckelberger, M. E., & De Wolf, S. (2023). Monolithic Perovskite/Silicon Tandems with >28% Efficiency: Role of Silicon-Surface Texture on Perovskite Properties. *Advanced Functional Materials*, 33(4), 2205557. <https://doi.org/10.1002/adfm.202205557>
 120. Roß, M., Severin, S., Stutz, M. B., Wagner, P., Köbler, H., Favine-Lévêque, M., Al-Ashouri, A., Korb, P., Tockhorn, P., Abate, A., Stannowski, B., Rech, B., & Albrecht, S. (2021). Co-Evaporated Formamidinium Lead Iodide Based Perovskites with 1000 h Constant Stability for Fully Textured Monolithic Perovskite/Silicon Tandem Solar Cells. *Advanced Energy Materials*, 11(35), 2101460. <https://doi.org/10.1002/aenm.202101460>
 121. Gil-Escrig, L., Susic, I., Doğan, İ., Zardetto, V., Najafi, M., Zhang, D., Veenstra, S., Sedani, S., Arikian, B., Yerci, S., Bolink, H. J., & Sessolo, M. (2023). Efficient and Thermally Stable Wide Bandgap Perovskite Solar Cells by Dual-Source Vacuum Deposition. *Advanced Functional Materials*, 33(31), 2214357. <https://doi.org/10.1002/adfm.202214357>
 122. Harter, A., Mariotti, S., Korte, L., Schlatmann, R., Albrecht, S., & Stannowski, B. (2023). Double-sided nano-textured surfaces for industry compatible high-performance silicon heterojunction and perovskite/silicon tandem solar cells. *Progress in Photovoltaics: Research and Applications*, 31(8), 813–823. <https://doi.org/10.1002/ppa.3685>
 123. Sahli, F., Kamino, B. A., Werner, J., Bräuninger, M., Paviet-Salomon, B., Barraud, L., Monnard, R., Seif, J. P., Tomasi, A., Jeangros, Q., Hessler-Wyser, A., De Wolf, S., Despeisse, M., Nicolay, S., Niesen, B., & Ballif, C. (2018). Improved Optics in Monolithic Perovskite/Silicon Tandem Solar Cells with a Nanocrystalline Silicon Recombination Junction. *Advanced Energy Materials*, 8(6), 1701609. <https://doi.org/10.1002/aenm.201701609>
 124. Mazzarella, L., Lin, Y., Kirner, S., Morales-Vilches, A. B., Korte, L., Albrecht, S., Crossland, E., Stannowski, B., Case, C., Snaith, H. J., & Schlatmann, R. (2019). Infrared Light Management Using a Nanocrystalline Silicon Oxide Interlayer in Monolithic Perovskite/Silicon Heterojunction Tandem Solar Cells with Efficiency above 25%. *Advanced Energy Materials*, 9(14), 1803241. <https://doi.org/10.1002/aenm.201803241>
 125. Zheng, J., Lau, C. F. J., Mehrvarz, H., Ma, F.-J., Jiang, Y., Deng, X., Soeriyadi, A., Kim, J., Zhang, M., Hu, L., Cui, X., Lee, D. S., Bing, J., Cho, Y., Chen, C., Green, M. A., Huang, S., &

- Ho-Baillie, A. W. Y. (2018). Large area efficient interface layer free monolithic perovskite/homo-junction-silicon tandem solar cell with over 20% efficiency. *Energy & Environmental Science*, *11*(9), 2432–2443. <https://doi.org/10.1039/C8EE00689J>
126. Zheng, X., Li, Z., Zhang, Y., Chen, M., Liu, T., Xiao, C., Gao, D., Patel, J. B., Kuciauskas, D., Magomedov, A., Scheidt, R. A., Wang, X., Harvey, S. P., Dai, Z., Zhang, C., Morales, D., Pruetz, H., Wieliczka, B. M., Kirmani, A. R., & Luther, J. M. (2023). Co-deposition of hole-selective contact and absorber for improving the processability of perovskite solar cells. *Nature Energy*, *8*(5), 462–472. <https://doi.org/10.1038/s41560-023-01227-6>
127. Puaud, A. (2021). *Understanding and Optimisation of transport mechanisms in Perovskite on Silicon Heterojunction Tandem Solar Cells* [Université Grenoble Alpes]. <https://theses.hal.science/tel-03462780>
128. Jäger, K., Sutter, J., Hammerschmidt, M., Schneider, P.-I., & Becker, C. (2021). Prospects of light management in perovskite/silicon tandem solar cells. *Nanophotonics*, *10*(8), 1991–2000. <https://doi.org/10.1515/nanoph-2020-0674>
129. Park, J., Kim, J., Yun, H.-S., Paik, M. J., Noh, E., Mun, H. J., Kim, M. G., Shin, T. J., & Seok, S. I. (2023). Controlled growth of perovskite layers with volatile alkylammonium chlorides. *Nature*. <https://doi.org/10.1038/s41586-023-05825-y>
130. Ye, S., Rao, H., Feng, M., Xi, L., Yen, Z., Seng, D. H. L., Xu, Q., Boothroyd, C., Chen, B., Guo, Y., Wang, B., Salim, T., Zhang, Q., He, H., Wang, Y., Xiao, X., Lam, Y. M., & Sum, T. C. (2023). Expanding the low-dimensional interface engineering toolbox for efficient perovskite solar cells. *Nature Energy*. <https://doi.org/10.1038/s41560-023-01204-z>
131. Muscarella, L. A., Petrova, D., Cervasio, R. J., Farawar, A., Lugier, O., McLure, C., Slaman, M. J., Wang, J., Hauff, E. von, & Williams, R. M. (2017). *Enhanced Grain-boundary Emission Lifetime and Additive Induced Crystal Orientation in One-Step Spin-Coated Mixed Cationic (FA/MA) Lead Perovskite Thin Films Stabilized by Zinc Iodide Doping*. <https://doi.org/10.26434/chemrxiv.5484073.v2>
132. Muscarella, L. A., Petrova, D., Jorge Cervasio, R., Farawar, A., Lugier, O., McLure, C., Slaman, M. J., Wang, J., Ehrler, B., von Hauff, E., & Williams, R. M. (2019). Air-Stable and Oriented Mixed Lead Halide Perovskite (FA/MA) by the One-Step Deposition Method Using Zinc Iodide and an Alkylammonium Additive. *ACS Applied Materials & Interfaces*, *11*(19), 17555–17562. <https://doi.org/10.1021/acsami.9b03810>
133. Kooijman, A., Muscarella, L. A., & Williams, R. M. (2019). Perovskite Thin Film Materials Stabilized and Enhanced by Zinc(II) Doping. *Applied Sciences*, *9*(8), 1678. <https://doi.org/10.3390/app9081678>
134. Yang, W. S., Park, B.-W., Jung, E. H., Jeon, N. J., Kim, Y. C., Lee, D. U., Shin, S. S., Seo, J., Kim, E. K., Noh, J. H., & Seok, S. I. (2017). Iodide management in formamidinium-lead-halide-based perovskite layers for efficient solar cells. *Science*, *356*(6345), 1376–1379. <https://doi.org/10.1126/science.aan2301>
135. Jeong, J., Kim, M., Seo, J., Lu, H., Ahlawat, P., Mishra, A., Yang, Y., Hope, M. A., Eickemeyer, F. T., Kim, M., Yoon, Y. J., Choi, I. W., Darwich, B. P., Choi, S. J., Jo, Y., Lee, J. H., Walker, B., Zakeeruddin, S. M., Emsley, L., & Kim, J. Y. (2021). Pseudo-halide anion engineering for α -FAPbI₃ perovskite solar cells. *Nature*, *592*(7854), 381–385. <https://doi.org/10.1038/s41586-021-03406-5>
136. Chi, W., Banerjee, S. K., Jayawardena, K. G. D. I., Silva, S. R. P., & Seok, S. I. (2023). Perovskite/Silicon Tandem Solar Cells: Choice of Bottom Devices and Recombination Layers. *ACS Energy Letters*, *8*(3), 1535–1550. <https://doi.org/10.1021/acsenergylett.2c02725>
137. Hoeksma, M.M., & Williams, R.M. (2023). Synergistic zinc(II) and formate doping of alpha-FAPbI₃ perovskite: Thermal stabilization and enhanced photoluminescence lifetime. Preprints. <https://doi.org/10.20944/preprints202311.0730.v1>

Springer Nature or its licensor (e.g. a society or other partner) holds exclusive rights to this article under a publishing agreement with the author(s) or other rightsholder(s); author self-archiving of the accepted manuscript version of this article is solely governed by the terms of such publishing agreement and applicable law.

Authors and Affiliations

Charles Marchant¹ · René M. Williams¹ 

✉ René M. Williams
r.m.williams@uva.nl

Charles Marchant
charles.marchant316@gmail.com

¹ Molecular Photonics Group, Van't Hoff Institute for Molecular Sciences (HIMS), Universiteit Van Amsterdam, Science Park 904, 1098 XH Amsterdam, Netherlands